

# Fast and Furious: Shock Heated Gas as the Origin of Spatially Resolved Hard X-ray Emission in the Central 5 kpc of the Galaxy Merger NGC 6240

Junfeng Wang<sup>1,2</sup>, Emanuele Nardini<sup>1,3</sup>, Giuseppina Fabbiano<sup>1</sup>, Margarita Karovska<sup>1</sup>, Martin Elvis<sup>1</sup>, Silvia Pellegrini<sup>4</sup>, Claire Max<sup>5</sup>, Guido Risaliti<sup>1,6</sup>, Vivian U<sup>7,8</sup>, Andreas Zezas<sup>1,9</sup>

jfwang@northwestern.edu

## ABSTRACT

We have obtained a deep, sub-arcsecond resolution X-ray image of the nuclear region of the luminous galaxy merger NGC 6240 with *Chandra*, which resolves the X-ray emission from the pair of active nuclei and the diffuse hot gas in great detail. We detect extended hard X-ray emission from  $kT \sim 6$  keV ( $\sim 70$  million K) hot gas over a spatial scale of 5 kpc, indicating the presence of fast shocks with velocity of  $\sim 2200$  km s<sup>-1</sup>. For the first time we obtain the spatial distribution of this highly ionized gas emitting Fe XXV, which shows a remarkable correspondence to the large scale morphology of H<sub>2</sub>(1-0) S(1) line emission and H $\alpha$  filaments. Propagation of fast shocks originated in the starburst driven wind into the ambient dense gas can account for this morphological correspondence. With an observed  $L_{0.5-8\text{keV}} = 5.3 \times 10^{41}$  erg s<sup>-1</sup>, the diffuse hard X-ray emission is  $\sim 100$  times more luminous than that observed in the classic starburst galaxy

---

<sup>1</sup>Harvard-Smithsonian Center for Astrophysics, 60 Garden St, Cambridge, MA 02138

<sup>2</sup>Center for Interdisciplinary Exploration and Research in Astrophysics (CIERA) and Department of Physics and Astronomy, Northwestern University, 2131 Tech Dr, Evanston, IL 60208

<sup>3</sup>*Current address:* Astrophysics Group, School of Physical and Geographical Sciences, Keele University, Keele, Staffordshire ST5 5BG, UK

<sup>4</sup>Dipartimento di Astronomia, Università di Bologna, Via Ranzani 1, 40127 Bologna, Italy

<sup>5</sup>Center for Adaptive Optics, University of California, 1156 High Street, Santa Cruz, CA 95064

<sup>6</sup>INAF-Arcetri Observatory, Largo E, Fermi 5, I-50125 Firenze, Italy

<sup>7</sup>Institute for Astronomy, University of Hawaii, 2680 Woodlawn Drive, Honolulu, HI 96822

<sup>8</sup>*Current address:* Department of Physics and Astronomy, University of California, Riverside, CA 92521

<sup>9</sup>Physics Department, University of Crete, P.O. Box 2208, GR-710 03, Heraklion, Crete, Greece

M82. Assuming a filling factor of 1% for the 70 MK temperature gas, we estimate its total mass ( $M_{\text{hot}} = 1.8 \times 10^8 M_{\odot}$ ) and thermal energy ( $E_{\text{th}} = 6.5 \times 10^{57}$  ergs). The total iron mass in the highly ionized plasma is  $M_{\text{Fe}} = 4.6 \times 10^5 M_{\odot}$ . Both the energetics and the iron mass in the hot gas are consistent with the expected injection from the supernovae explosion during the starburst that is commensurate with its high star formation rate. No evidence for fluorescent Fe I emission is found in the CO filament connecting the two nuclei.

*Subject headings:* X-rays: galaxies — galaxies: starburst — galaxies: interactions — galaxies: ISM — galaxies: individual (NGC 6240)

## 1. Introduction

In the local universe, NGC 6240 ( $z=0.02448 \pm 0.00003$ ; Downes et al. 1993) is a unique galaxy, in the throes of a violent merging event and on its way to becoming an elliptical galaxy (Tacconi et al. 1999; Tecza et al. 2000; Bush et al. 2008; Engel et al. 2010; Medling et al. 2011). It is experiencing intense star formation (e.g.,  $61 \pm 30 M_{\odot} \text{ yr}^{-1}$  in Yun & Carilli 2002;  $25 M_{\odot} \text{ yr}^{-1}$  in Engel et al. 2010). With  $L_{\text{FIR}} \sim 10^{11.8} L_{\odot}$  just below  $10^{12} L_{\odot}$ , the luminosity threshold for the ultraluminous infrared galaxies (ULIRGs, Sanders & Mirabel 1996; Genzel et al. 1998), NGC 6240 is expected to become an ULIRG when the galaxies coalesce and a final starburst is triggered (Engel et al. 2010).

The *Chandra* X-ray images (Lira et al. 2002; Komossa et al. 2003) of the central region of NGC 6240 revealed two gravitationally interacting active supermassive black holes (SMBHs) separated by  $1.5''$  ( $\sim 0.7$  kpc). These sources are characterized by the highly absorbed hard X-ray spectra typical of Compton thick active galactic nuclei (AGNs; Iwasawa & Comastri 1998; Matt et al. 2000). They each have an observed luminosity of  $L_{2-8\text{keV}} \sim 10^{42} \text{ erg s}^{-1}$ , and show prominent neutral Fe  $K\alpha$  lines at 6.4 keV present in the spectra of both nuclei (Komossa et al. 2003).

Limited by the number of counts, marginal evidence of an H-like Fe line in the spectral fit and extended hard X-ray emission in the morphology was also suggested by Komossa et al. (2003). This line emission could be associated with a spatially resolved, multi-temperature hot gas outflow, powered by the starburst activity that dominates the 0.5-3 keV X-ray emission ( $L_{0.1-2\text{keV}} \sim 10^{43} \text{ erg s}^{-1}$ ; Schulz et al. 1998; Komossa et al. 2003; Ptak et al. 2003; Huo et al. 2004; Grimes et al. 2005). *XMM-Newton* observations (Boller et al. 2003; Netzer et al. 2005) resolved the Fe K line complex into three narrow lines, the neutral Fe  $K\alpha$ , Fe XXV, and a blend of Fe XXVI with Fe  $K\beta$ . Using a three-zone model, Netzer et al.

(2005) further identified that the emission lines of higher ionization ions (e.g., Fe XXV line) originated from the inner 2.1 kpc region. These *XMM-Newton* data, however, do not have the resolution to resolve spatially the line-emitting regions.

In this paper, we focus on the spatially resolved 5.5-8 keV X-ray emission of the innermost central  $\sim 5$  kpc ( $\sim 10''$ ) region in NGC 6240 based on new, and archival, *Chandra* imaging. This choice of hard energy range allows us to investigate the origin of the high temperature gas and the highly ionized iron emission. A detailed study of the extended soft X-ray halo has been presented in a companion paper (Nardini et al. 2013). A third paper (Wang et al. 2013, in preparation) will discuss the extended soft X-ray emission in the  $r \lesssim 15''$  region. Taking advantage of the order of magnitude deeper imaging, along with sub-pixel resolution, we are able to firmly establish the presence and the spatial distribution of the hard X-ray emission. Throughout this work we adopt a luminosity distance of  $D_L = 107$  Mpc to NGC 6240 ( $1'' = 492$  pc), based on the concordance cosmological parameters ( $H_0 = 70.5$  km s $^{-1}$  Mpc $^{-1}$ ,  $\Omega_m = 0.27$ ,  $\Omega_\Lambda = 0.73$ ; Komatsu et al. 2011).

## 2. Observations and Data Reduction

NGC 6240 was observed on May 31, 2011 with the *Chandra* Advanced CCD Imaging Spectrometer (ACIS; Garmire et al. 2003) for 146 ks (ObsID 12713, PI: Fabbiano). The binary nucleus of NGC 6240 was placed near the nominal aimpoint of the backside-illuminated, low energy sensitive S3 chip. The ACIS data were reprocessed<sup>1</sup> with the *Chandra* Interactive Analysis of Observations software package (CIAO; version 4.4) using the latest *Chandra* Calibration Database (CALDB) version 4.5.1. The net exposure time was 144 ks after screening for brief periods of elevated background. The archival ACIS S3 observation (ObsID 1590, previously presented in Komossa et al. 2003) shown in this work was taken on February 22, 2002 with a total exposure of 37 ks. We reprocessed the ACIS data to generate a new level 2 event file that has the latest calibration and the subpixel resolution algorithm (“EDSER”, Li et al. 2003) applied. We checked for X-ray counterparts of the optical and near infrared point sources in the field of view using the Naval Observatory Merged Astrometric Dataset catalog (NOMAD; Zacharias et al. 2004), and compared the positions of all the bright point-like X-ray sources across the observations. We verified the accuracy of the absolute astrometry to within  $<1$  native pixel (0.492 arcsec), thus no further relative offsets were applied. The event files were all reprojected to the coordinate frame of ObsID 12713, and the four images were merged using CIAO tools `reproject_events` and `dmmerge`. Because

---

<sup>1</sup><http://cxc.harvard.edu/ciao/threads/createL2/>

the effective area of the *Chandra* High Energy Transmission Grating (HETG) zeroth-order image is about 60% of ACIS-S at 6.4 keV, we also make use of two archival deep HETG observations (PI: Canizares; ObsID 6908, 159 ks, observed on May 16, 2006; ObsID 6909, 143 ks, observed on May 11, 2006), providing an equivalent of 180 ks ACIS-S imaging in the Fe K band. Therefore, the combined depth of our imaging data reaches  $\sim 363$  ks, which improves by an order of magnitude over the first ACIS image of NGC 6240 (Komossa et al. 2003) in the 5.5-8 keV range. The first-order *Chandra* HEG spectrum is quite faint, which was previously presented in Shu et al. (2011) but only focused on measurement of the intrinsic width of the neutral iron  $K\alpha$  emission line. We obtained the HEG spectra from the TGCat database (<http://tgcats.mit.edu/>) and combined the first orders of the grating data (the positive and negative arms). The extraction aperture was  $r = 4$  arcsec centered on the brighter northern nucleus. Given the complex diffuse emission, using a larger extraction window will yield unreliable Redistribution Matrix File (RMF) because of blurring of spatial-spectral information along the dispersion direction. For reference, the spectral resolution of HEG is  $\Delta E = 0.041$  keV at 6.4 keV ( $\Delta\lambda = 0.012\text{\AA}^2$ , FWHM) and the systematic uncertainty in the HEG wavelength calibration<sup>3</sup> is  $\sim 0.01$  keV ( $\sim 430$  km s<sup>-1</sup>) at 6.4 keV. Table 1 summarizes the *Chandra* ACIS and HETG observations used in our work.

### 3. Imaging Spectroscopic Analysis of the NGC 6240 Central Region

Figure 1 shows the *Chandra* ACIS image of the inner  $25'' \times 25''$  ( $\sim 12$  kpc across) region of NGC 6240 in the 5.5-8 keV band extracted from the merged data, together with an archival *HST* ACS/WFC F814W image (Cycle 14 program 10592, PI: A. Evans), highlighting the highly disturbed optical morphology of NGC 6240. The two nuclei are resolved as the brightest X-ray point sources in the center, with peak emission separated by  $1.5''$  (710 pc), matching the nuclear compact radio source positions (e.g., N1 and N2 in the 8.4 GHz map of Colbert et al. 1994; N1 and S in the 1.4 and 5 GHz maps of Beswick et al. 2001; North and South black hole positions in Max et al. 2007).

Diffuse emission is clearly present (Figure 1b), extending to  $r = 10''$  ( $\sim 5$  kpc). Hereafter we refer this region as the central region of NGC 6240. The X-ray morphology resembles a “heart” with loop-like features in the south, the north-east, and the north-west directions (Figure 1b). A comparison between the observed surface brightness profile and that of a point source further confirms the presence of significant hard X-ray emission reaching

---

<sup>2</sup><http://cxc.harvard.edu/proposer/POG/html/HETG.html>

<sup>3</sup><http://space.mit.edu/CXC/calib/hetgcal.html>

$r \sim 10''$  radial distance. Figure 2 shows the excess of hard X-rays over the scattered emission in the wings of the point spread function (PSF). The radial profile flattens past  $10''$ , where background emission dominates. The *Chandra* PSF shown in Figure 2 was created simulating a point source at the same position on the detector as the center of NGC 6240 in the single observation of the longest exposure (ObsID 12713) using the *Chandra* Ray Tracer (ChaRT<sup>4</sup>) and the MARX<sup>5</sup> simulator. This PSF was then rescaled to match the combined 5.5-8 keV counts from the two nuclei. Since the nuclei are separated by  $1.5''$ , and we are interested in demonstrating the presence of extended emission several arcseconds from the nuclei, this is an adequate procedure. For the investigation of extended emission close to the nuclei (e.g., between the nuclei), we have performed a more complex 2-D image fitting with two PSF components, described in the next section.

### 3.1. Spectral Analysis: Neutral, He-like and H-like Fe K lines

Previous work by Boller et al. (2003) identified ionized Fe K emission lines from the presence of a collisionally ionized plasma with a temperature  $kT = 5.5 \pm 1.5$  keV, producing the Fe XXV (at 6.7 keV) and Fe XXVI (at 6.93 keV)  $K\alpha$  recombination lines. Boller et al. also inserted in their fit the neutral or low ionization Fe  $K\alpha$  line (expected at 6.4 keV) and  $K\beta$  line (at 7.058 keV), each modelled with a Gaussian line. Such fluorescent lines of large (up to few keV) equivalent widths (EWs) arise from large column density gas which strongly attenuates directly viewed X-rays from the AGNs.

To shed light on the spectral properties of the spatially resolved central region, we extracted the spectra of both nuclei and all the emission in the  $10''$ -radius circle. Figure 3a compares the ACIS spectra of the central region of NGC 6240 (circle in Figure 1, all emission within  $r=10''$ ,  $\sim 5$  kpc from the nuclei) and the innermost region containing the two nuclei (ellipse in Figure 1, full lengths of the axes  $4'' \times 2''$ ).

The complex Fe K line structure detected in *XMM-Newton* spectra (Boller et al. 2003; Netzer et al. 2005) is clearly present in the *Chandra* ACIS spectra (Figure 3) and contributes most counts, in contrast to the low continuum in the same region. Approximately 80% of this continuum comes from the innermost region enclosing the nuclei. There are notable differences between the two spectra, which are further illustrated in Figure 3 showing the residual spectrum excluding the nuclei. Following Boller et al. (2003), we added four narrow

---

<sup>4</sup><http://cxc.harvard.edu/chart/>

<sup>5</sup>Version 4.4.0; <http://space.mit.edu/cxc/marx/>

Gaussian emission lines (representing neutral Fe  $K\alpha$ , Fe XXV, Fe XXVI, and Fe  $K\beta$ ) to a highly absorbed power law continuum to fit the spatially resolved spectra (the northern nucleus, the southern nucleus, and the extended emission within  $r = 10''$ , i.e., nuclei+diffuse). This phenomenological approach is adopted to identify the spatial distribution of the line emission, and a more physically meaningful model will be used in the later section. To prevent over-subtraction of diffuse emission from the hot gas in the nuclear region, we did not exclude the innermost region when evaluating the hot gas content in the  $r \leq 10''$  emission; instead, we included nuclear components to represent the contribution from the AGNs.

Figure 3 also shows a hint for two peaks in the Fe XXV line, which resembles double peaked emission line profiles seen in the optical spectra of AGN with bi-conical outflows (e.g. Mrk 78, Whittle & Wilson 2004). However, it is statistically insignificant: the probability that the model with one more gaussian component improves over the current fit is only 80% based on a likelihood ratio test (10000 simulations) performed using XSPEC. In fact, the energy resolution of the ACIS S3 detector is 0.2 keV<sup>6</sup> (FWHM) at 6.4 keV whereas the apparent double peaks are separated by 0.05 keV, therefore we suggest that it is not a real resolved feature. The Fe XXVI and  $K\beta$  lines are blended together at the spectral resolution of the ACIS CCD, therefore we fixed the  $K\beta$  line center energy at 7.058 keV (rest frame) and scaled the line intensity according to the theoretical ratio (1/8.8, e.g., Palmeri et al. 2003) relative to the  $K\alpha$  line. The best-fit centroid energies, EWs, and line fluxes, and associated 1- $\sigma$  errors are summarized in Table 2.

Although the first-order *Chandra* HEG spectrum is faint, we attempted to spectroscopically resolve the various Fe features. The grating spectrum was rebinned for a minimum S/N ratio of 3 and was fitted with the similar model consisting of an absorbed power law continuum plus gaussian lines using XSPEC. Again we caution that the best-fit value of  $\Gamma$  for the simplistic power law continuum model is not physically meaningful but simply parameterization. We recovered a  $FWHM = 2860 \pm 550$  km s<sup>-1</sup> for the Fe $K\alpha$  6.4 keV line, consistent with the  $FWHM \sim 2810$  km s<sup>-1</sup> reported in Shu et al. (2011). Interestingly, the FeXXV line at 6.7 keV is marginally resolved at  $2.4\sigma$  significance with the measured  $FWHM = 5550_{-1390}^{+1670}$  km s<sup>-1</sup>, implying a large velocity range in the hot gas kinematics. Furthermore, the HEG spectrum does not resolve this line into two peaks, although it shows the line is broad ( $FWHM \sim 5550$  km s<sup>-1</sup>). More counts would have allowed finer binning to attempt resolving the broad line into two or more kinematic components.

The line fluxes further confirm that the Fe XXV emission is spatially extended while the neutral Fe  $K\alpha$  emission is concentrated at the nuclei. The neutral or weakly ionized

---

<sup>6</sup><http://cxc.harvard.edu/proposer/POG/html/chap6.html>

Fe  $K\alpha$  line emission at 6.4 keV (centered at 6.25 keV in the observer frame) is also mostly associated with the nuclei, with  $\sim 15\%$  of the total Fe I  $K\alpha$  emission in the extended region (Figure 3). At the 6.4 keV energy, the PSF scattering of nuclear emission to the larger radii cannot be neglected, which is  $\sim 10\%$ . Taking this into account, the spatially extended Fe I  $K\alpha$  emission is at 5% of the total. The Fe XXVI emission is fully accounted for by the innermost nuclear emission, indicating that the mostly ionized H-like iron is confined in this region. In contrast,  $\sim 30\%$  of Fe XXV line emission appears to originate in the extended region outside of the nuclear region (taking into account of the PSF contribution). In the following we will investigate the morphology of this emission. Given that the XMM spectra (Netzer et al. 2005) come from a larger region, the similarity of the fluxes with our *Chandra* measurements excludes significant Fe emission beyond  $r = 10''$ .

### 3.2. Narrow-band Hard X-ray Images

The analysis above shows that the AGNs alone in NGC 6240 cannot account for the observed Fe K complex, except for the Fe  $K\alpha$  and  $K\beta$  emission (the latter fainter and blended with Fe XXVI), which is due to fluorescence of neutral or low ionization material near the AGNs. Guided by the spectra (Figures 3 and 4), we extracted *Chandra* narrow-band line images to investigate the morphology of the emission line gas.

Figure 5 shows images in the 5.5-6 keV continuum band that is free from any significant line emission, the Fe  $K\alpha$  line (6-6.4 keV) and the Fe XXV line (6.4-6.7 keV). The blended Fe XXVI and Fe I  $K\beta$  emission was examined but not shown here, since it does not show any evidence for emission beyond the nuclear region. Although the line emission dominates in these narrow bands, the contribution of the continuum has been removed from the images regardless, assuming a single power law with a photon index ( $\Gamma = 0.8$ ) from the spectral fit of the continuum in the central region. The contribution from the continuum in the emission line bands is calculated using the photon index and the counts in 5.5-6.0 keV, taking into account the difference in the effective areas. Given that the starburst likely dominates the extended emission (e.g., Netzer et al. 2005), we further confirmed that the following results do not change adopting a thermal bremsstrahlung spectrum ( $kT \sim 6$  keV for the hot gas) to approximate the flat continuum.

The continuum-subtracted line emission images clearly show that the 6.4 keV Fe I  $K\alpha$  line peaks at the dual nuclei, with weak emission extending to  $r = 3''$  from the nuclei and contributing  $\sim 10\%$  of the total  $\sim 900$  Fe  $K\alpha$  counts. The Fe XXV emission is also centrally peaked at the nuclear region with a dominating southern nucleus, but it appears more extended to the southwest and to the east; the  $r = 10''$  region outside of the nuclei

contains  $\sim 40\%$  of the  $\sim 500$  total Fe XXV counts. These values are in good agreement with the results from spectral analysis above.

To extract more morphological information from the data, we performed image restoration using the Expectation through Markov Chain Monte Carlo (EMC2) algorithm (Esch et al. 2004; Karovska et al. 2005). The effectiveness of this method with *Chandra* images was demonstrated with a number of astronomical imaging studies (Karovska et al. 2005, 2007; Wang et al. 2009a, 2012). The EMC2 deconvolution is more effective for preserving diffuse features compared to other PSF-deconvolution algorithms (e.g., Lucy 1974). Only the single deep imaging observation (ObsID 12713) and the associated PSF were used to minimize the PSF variations across multiple observations. The PSF-deconvolved images, shown in Figure 6, provide the highest resolution view of the central region. In particular, the faint diffuse Fe XXV emission is more obvious in Figure 6c.

### 3.3. Sub-kpc-scale Extended Emission between the Nuclei

Close examination of the images suggests the possibility of some extended hard X-ray emission in the region between the two nuclei, especially in the Fe XXV band (and perhaps in the Fe  $K\alpha$  band; see Figures 5 and 6). However, evaluating the significance of this emission is very difficult because of the close separation ( $1.5''$ ) of the nuclei. The PSF wings of the two X-ray point sources overlap in this region and enhance the emission here, which needs to be taken into account. Simulating two point sources convolved with the PSF, we performed 2-D image fitting to subtract the PSF<sup>7</sup> on the 5.5-8 keV image, as well as individual narrow band images, using *Sherpa*<sup>8</sup>. The results are shown in Figure 7. For the 5.5-8 keV image that has most counts, besides the clear extension to the southwest and the northeast (already noted above as the extended central region), the residual image further indicates that there is extended emission in the region between the two nuclei, immediate north of the southern nucleus, at  $\sim 10 \sigma$  significance level when evaluated using a  $1'' \times 1''$  box region. For the narrow band images, the statistics are poorer; nevertheless, this extended feature is seen in all three residual images. Its significance ranges from  $\sim 6 \sigma$  in the Fe XXV line emission to  $\sim 3 \sigma$  in the Fe  $K\alpha$  line emission.

We further checked for possible contamination from the PSF artifact<sup>9</sup> found in ACIS

---

<sup>7</sup>See detailed procedure available at <http://cxc.harvard.edu/sherpa4.4/threads/2dpsf/>.

<sup>8</sup>Version 2 in CIAO 4.4; <http://cxc.harvard.edu/sherpa/>

<sup>9</sup>[http://cxc.harvard.edu/ciao4.4/caveats/psf\\_artifact.html](http://cxc.harvard.edu/ciao4.4/caveats/psf_artifact.html)

data. Using the CIAO tool `make_psf_asymmetry_region`, this artifact should lie in position angle  $0 - 50^\circ$  in our data. Given that this PSF asymmetry feature may contain only 5% of the flux<sup>10</sup>, it would have in any case minimal impact on our results.

### 3.4. Comparison with Multiwavelength Images

In this section, we compare the hard X-ray morphology of the center of NGC 6240 with a number of high spatial resolution images available in other wavelength ranges, aiming to find clues for the physical origin of the extended X-ray emitting gas. The absolute astrometry of our *Chandra* ACIS image is excellent, indicated by the agreement between the coordinates of the X-ray and the radio nuclei ( $\sim 0.2''$  accuracy, see Max et al. 2007 for a further astrometry discussion).

We first compare the 5.5-8 keV emission with the optical  $H\alpha$  emission morphology from *HST*/WFPC2 F673N image (Lira et al. 2002), as shown in Figure 8a. The 5.5-8 keV image was adaptively smoothed with CIAO tool `dmimgadapt` using a Gaussian kernel with smoothing scales of 1 pixel to 20 pixels, to better visualize structures in the diffuse emission. As a separate approach, the same 5.5-8 keV image with the PSF deconvolution applied is also shown in Figure 8b. The optical peaks are not aligned with the X-ray nuclei due to obscuration. Lira et al. (2002) and Komossa et al. (2003) have previously shown that on  $10''$  (4.9 kpc) scale, the  $H\alpha$  emission and the soft X-ray emission share a similar morphology consisting of filaments and loops. The overall morphology of the soft X-ray emission in our deep image (Wang et al. 2013) is similar to that shown in Komossa et al. (2003) but with finer structure details, closely following the optical  $H\alpha$  emission. Such morphological correspondence is seen but less obvious in the hard X-ray emission, except for the bright  $H\alpha$  filament to the east and the loop to the northwest of the nuclei. Figure 8c and 8d further compare the  $H\alpha$  morphology with images in the 5.5-6 keV continuum band and the Fe XXV band. A close morphological correspondence between the  $H\alpha$  and the hard X-rays can be found at the base of an incomplete loop to the west of the nuclei (Figure 8c and d), and at the filament to the south and east of the southern nucleus (Figure 8d).

Next we compare the 5.5-8 keV image with the [FeII]  $1.644 \mu\text{m}$  line emission (van der Werf et al. 1993) in Figure 9. The [FeII] emission in NGC 6240 could be produced by shocks in supernova remnants (SNRs; see van der Werf et al. 1993 for detailed discussion on possible excitation mechanisms), and is brightest at the locations of the two nuclei, consistent with the presence

---

<sup>10</sup>See document written by Vinay Kashyap (CXC) available at [http://cxc.harvard.edu/cal/Hrc/PSF/acis\\_psf\\_2010oct.html](http://cxc.harvard.edu/cal/Hrc/PSF/acis_psf_2010oct.html)

of nuclear starbursts (Engel et al. 2010). The two [FeII] emission peaks fall close to the X-ray nuclei, with a slight offset ( $0.2''$ ) to the north relative to the X-ray northern nucleus.

We find a close correlation of the spatially extended Fe XXV emission with the near IR H<sub>2</sub>(1-0) 2.12  $\mu\text{m}$  emission obtained with Keck II (Max et al. 2005). Previous work (van der Werf et al. 1993; Max et al. 2005) noted that the H<sub>2</sub>(1-0) emission in NGC 6240 does not follow the stellar light but peaks between the two nuclei, which is thought to be excited by shocks (Moorwood & Oliva 1988; van der Werf et al. 1993). To compare H<sub>2</sub> and our X-ray images, the astrometry of the H<sub>2</sub> image was first registered using an IR-bright star (2MASS J16530119+0224138,  $K=10.4$  mag) in the field. Figure 10 shows a remarkably good correspondence between the observed (top panel), and especially the deconvolved (lower panel) Fe XXV line emission and the H<sub>2</sub>(1-0) 2.12  $\mu\text{m}$  emission.

Finally we compare the Fe I  $K\alpha$  emission with the cold molecular gas distribution in the nuclear region, traced by the CO(3-2) emission obtained with the Submillimeter Array (SMA) from U et al. (2011). Figures 11a and 11b show that the CO emission resembles a ‘bridge’ or filament between the two nuclei, with the bright peak offset to the north of the southern Fe I  $K\alpha$  peak. The evidence for fluorescent Fe I emission from this cold gas is marginal at most, with Fe  $K\alpha$  emission extending to the north of the southern nucleus at  $3\sigma$  significance level.

### 3.5. Spectral Fit with Thermal Plasma Model

To extract the physical parameters of the highly ionized gas responsible for the Fe XXV and Fe XXVI emission, we fitted the 5.5–9 keV spectra of the  $r \leq 10''$  region. The contribution from the lower temperature gas (e.g.,  $kT = 0.7$  keV and  $kT = 1.4$  keV components; Boller et al. 2003) found in previous studies is negligible in this energy range. We adopted an absorbed single temperature thermal plasma (*APEC*; Smith et al. 2001) model for the collisionally ionized gas producing the highly ionized Fe XXV and Fe XXVI emission lines, plus zero-width Gaussian lines centered at 6.400 keV and 7.058 keV (rest frame) as the neutral Fe  $K\alpha$  and  $K\beta$  lines, respectively. A photoionized origin for the Fe XXV was not considered as this was previously ruled out by the detailed photoionization calculation given by Netzer et al. (2005). The continuum contribution from the two nuclei is accounted for by including an absorbed power law component, representing the reflected nuclear emission. The gaussian line components were also subject to this absorption column. The absorption column ( $N_H = 4 \times 10^{23} \text{ cm}^{-2}$ ), the photon index ( $\Gamma = 0.9$ ) and the normalization ( $A = 1.5 \times 10^{-4}$ ) are fixed to be the best fit values combining the two nuclei. The abundance  $Z$  is fixed at solar values (Grevesse & Sauval 1998).

The spectrum with the best-fit model is plotted in Figure 12, which is well represented with a  $\chi^2/d.o.f = 300/246$ . The temperature of the hot plasma is  $6.15 \pm 0.33$  keV with an absorption column of  $N_H = 5.5 \pm 1.7 \times 10^{23}$  cm $^{-2}$ . The observed 0.5–8 keV luminosity is  $5.3 \pm 1.0 \times 10^{41}$  erg s $^{-1}$  and  $L_{0.5-8\text{keV}} = 5.5 \pm 1.4 \times 10^{42}$  erg s $^{-1}$  after correction for absorption. The normalization is  $2.5 \pm 0.5 \times 10^{-3}$ , in units of  $[10^{-14}/(4\pi(D_A(1+z))^2) \int n_e n_H dV]$ , where  $D_A$  is the angular size distance to NGC 6240 (cm),  $n_e$  is the electron density (cm $^{-3}$ ), and  $n_H$  the hydrogen density (cm $^{-3}$ ). We obtain an emission measure (E.M.  $\equiv \int n_e n_H dV$ ) of  $3.1 \times 10^{65} \eta$  cm $^{-3}$ , where  $\eta$  is a volume filling factor.

It is unlikely that all the hot plasma emission is affected by a high column, given the clumpy morphology and the spatial extent. Fortunately, because we are working in the hard X-ray range, the absorption corrected luminosity is less vulnerable to the uncertainty in the absorption column. Previous studies (Boller et al. 2003) and the broad band fit indicate an absorption column of  $N_H = 4.1 \times 10^{22}$  cm $^{-2}$  is reasonable outside of the nuclear region. This implies that our absorption corrected luminosity could be over-estimated by a factor of 2 (or 0.3 dex in  $\log L_x$ ). To investigate the impact of the soft X-ray thermal components that are clearly present (Komossa et al. 2003, Netzer et al. 2005), we modeled the broad band spectrum of the extended emission (the same  $r \leq 10''$  region). Figure 13 shows the 0.3–8 keV band ACIS spectrum (grating zero-order spectra were not combined because of low effective area in the soft X-ray band; see discussion in Nardini et al. 2013). The best fit model components are overplotted including two more thermal components with lower temperature ( $kT_1 = 1.03$  keV,  $kT_2 = 1.56$  keV), each subjected to an absorption column ( $N_{H,1} = 3.3 \times 10^{21}$  cm $^{-2}$ ,  $N_{H,2} = 5.3 \times 10^{22}$  cm $^{-2}$ ). The high temperature component has a similar  $kT_3 = 6.0$  keV that is consistent with the previous fitted value. Fixing their abundances at solar values gives statistically unacceptable fit ( $\chi_\nu > 3$ ) and allowing for variation relative to solar abundance improves the fit to ( $\chi_\nu = 1.32$ ). Remaining residuals are a few peaks higher than model predicted line emission at line energies corresponding to MgXII (rest frame 1.47 keV), SiXIV (2.01 keV) and SXVI (2.62 keV), indicating likely anomalous abundances for these elements. Indeed Netzer et al. (2005) suggested these elements have  $\sim 2$  times higher abundance. A word of caution is that the soft X-ray emission over a large spatial scale suffers from blending of thermal plasma of inhomogeneous absorption, temperature, and abundance, therefore spatially resolved studies in small regions is preferred. For our purpose of evaluating the contamination from these components to the hard energy range, we only add in gaussian lines to improve the fit ( $\chi_\nu = 1.18$ ) which are shown in Figure 13. We evaluated that the declining hard tails of the soft X-ray spectral components only contaminate the 5.5–8 keV spectral range at 8% level, which has a minimal impact on the derived  $N_H$  ( $4.0 \pm 0.3 \times 10^{23}$  cm $^{-2}$  when the hard tails from the softer X-ray components are accounted for).

Using the Fe XXV line emission as a tracer for the extent of the hottest thermal com-

ponent, which is confined within the central  $r = 10''$ , we can obtain the volume of the thermal gas emitting hard X-rays,  $V = 1.5 \times 10^{67} \eta \text{ cm}^3$ , assuming a spherical geometry. This implies  $n_e = 0.15 \eta^{-\frac{1}{2}} \text{ cm}^{-3}$ . Following the calculations done in Richings et al. (2010), the 70 million K gas contains a total mass of  $M_{hot} = 1.8 \times 10^9 \eta^{\frac{1}{2}} M_\odot$  and a thermal energy of  $E_{th} = 6.5 \times 10^{58} \eta^{\frac{1}{2}} \text{ ergs}$ . Since we assumed solar abundance, this implies the total iron mass in the highly ionized plasma  $4.6 \times 10^6 \eta^{\frac{1}{2}} M_\odot$ . Note that we also explored fitting with abundance left free and the best fit model gives  $Z = 0.5_{-0.2}^{+0.3} Z_\odot$  with a lower  $kT = 4.9 \pm 1.1 \text{ keV}$ , which has minor impact on the above estimated values. In addition, there is a degeneracy between the flat powerlaw component (which is most effectively constrained by the very hard end of the spectrum) and the hot thermal component (most effectively constrained by the Fe XXV line assuming fixed solar abundance). We find that a 0.05 dex increase in the normalization for the powerlaw component corresponds to a 0.09 dex decrease in the thermal component. When non-solar abundance is allowed, it leads to a 0.19 dex decrease in the normalization for the thermal component. This has negligible impact to our discussion later on the energetics of the hot gas.

The filling factor of the hot gas is poorly constrained observationally. Nevertheless, hydrodynamic simulations by Strickland & Stevens (2000) suggest that  $\eta$  ranges between 0.1% to 10% for X-ray bright galactic winds. In the starburst region  $\eta$  is considered to be higher than in the large scale wind, close to 100% (Strickland & Heckman 2007). To facilitate our discussion, we assume  $\eta \sim 1\%$  and caution the large uncertainty on this value. We consider that this is reasonable average value for the large volume spanned by the hot gas; the true filling factor is most probably close to unity in the innermost X-ray brightest region and  $\ll 1\%$  in the outer sphere. However, we also note that the dependence on  $\eta$  is relatively weak for the hot gas mass and thermal energy ( $\eta^{\frac{1}{2}}$ ).

#### 4. Discussion: Origin of the Diffuse Hard X-rays

We have unambiguously detected diffuse hard (5.5-8 keV) X-ray emission in the central region of the merging galaxy NGC 6240. The Fe  $K\alpha$  and  $K\beta$  fluorescent lines in NGC 6240 have been firmly associated with the photoionized gas of high column density and low ionization close to the AGN (e.g., Komossa et al. 2003, Netzer et al. 2005). Most of the observed Fe I line flux is explained by the emission from the NGC 6240 nuclei, and the spatial concentration at the nuclear positions is consistent with this interpretation. Even with the long exposure, we do not find strong evidence that the dense molecular clouds in the nuclear region are producing fluorescent Fe lines. The excess of Fe I  $K\alpha$  counts in the CO bridge between the nuclei (Figure 11) is marginal ( $3\sigma$  significance) when the scattered

counts from both AGN are excluded.

What is the origin of the highly ionized gas emitting the Fe XXV line that extends over 5 kpc in NGC 6240? Given the LIRG nature of NGC 6240 characterised by a high SFR ( $25 M_{\odot} \text{ yr}^{-1}$ , Engel et al. 2010), we first estimate the contribution to hard X-ray emission by the ensemble of X-ray binary (XRB) systems in the starburst. Using the correlation between the galaxy-wide 2–10 keV luminosity and the SFR provided by the *Chandra* survey of LIRGs (Lehmer et al. 2010, Table 4), the expected  $L_{HX}^{gal}$  from the XRB population is  $3.3 \times 10^{40} \text{ erg s}^{-1}$  in the 2–10 keV band, adopting a  $SFR \sim 25 M_{\odot} \text{ yr}^{-1}$  (Engel et al. 2010). This is only 5% of the observed 2–10 keV luminosity of the extended hard X-ray emission, strongly indicating that the diffuse emission is dominated by hot gas. Such hard X-ray emission is most likely associated with the thermal gas from merged supernova (SN) ejecta and stellar winds present during a starburst. The He-like Fe XXV line emission is also observed in other well known starburst galaxies like NGC 253 and M82 (e.g. Pietsch et al. 2001; Mitsuishi et al. 2011), the ULIRG Arp 220 (Iwasawa et al. 2005), and the integrated spectrum of a number of LIRG/ULIRG systems (Iwasawa et al. 2009), suggesting the existence of similar high temperature plasma. It is worth noting that the observed diffuse hard X-ray emission in NGC 6240 here is almost 100 times more luminous than that observed in the classic superwind system M82 ( $L_{2-8\text{keV}} = 4 \times 10^{39} \text{ erg s}^{-1}$ ; Strickland & Heckman 2007).

Using optical imaging and spectroscopy to identify outflow in the warm ionized medium, Heckman et al. (1990) have shown NGC 6240 to host a superwind. Superwinds are believed to be driven by the thermal and ram pressure of an initially very hot ( $T \sim 10^8 \text{ K}$ ), high-pressure ( $P/k \sim 10^7 \text{ K cm}^{-3}$ ) and low-density wind. According to the starburst driven superwind model, a hot gas bubble of internally shocked wind material with a temperature of several keV forms in the region of intense starformation (Chevalier & Clegg 1985, Suchkov et al. 1994, Strickland & Heckman 2007); this hot gas eventually flows outward as a high-speed (few  $1000 \text{ km s}^{-1}$ ) wind. Here we detected and spatially constrained for the first time thermal X-ray emission from such hot ( $T \sim 70 \text{ MK}$ ) gas in NGC 6240, likely the thermalized SN ejecta within the vicinity of the starburst region.

To further investigate whether the thermal energy content of the hot gas could be powered by thermalization of SNe shocks, we need to estimate the kinetic energy input from the SNe during the starburst. The resulting heating by SNe shocks should at least be comparable to  $E_{th}$ , considering that there are lower temperature phases and the gas has also bulk kinetic energy. The most often quoted SN rate for NGC 6240 is  $\sim 2 \text{ yr}^{-1}$  (e.g., van der Werf et al. 1993; Beswick et al. 2001; Pollack et al. 2007), which will be used next, although we note there is a small range of estimates. Engel et al. (2010) calculated a lower SN rate of  $0.3 \text{ yr}^{-1}$  assuming 20 Myr of continuous star formation at  $25 M_{\odot} \text{ yr}^{-1}$ , based on

the measured K-band luminosity. Using the correlation between [FeII] 1.257  $\mu\text{m}$  and the SN rate recently found by Rosenberg et al. (2012) from a sample of nearby starburst galaxies (Equation 2 and Figure 9 therein), we find a higher but comparable SN rate ( $\sim 3 \text{ yr}^{-1}$ ). Assuming a fraction ( $\alpha = 0.1$ , Chevalier & Clegg 1985, Thornton et al. 1998) of the kinetic energy input ( $10^{51}$  ergs per SN) is converted into thermal energy of the hot gas, the total energy deposited during the past  $\Delta t_{SB} \sim 20$  Myr of most recent starburst (Tecza et al. 2000) is  $E = 4 \times 10^{57}$  ergs, which is comparable to  $E_{th} = 6.5 \times 10^{57}$  ergs. Adopting a 10% filling factor for the hot gas results in a larger  $E_{th}$  and a larger deficiency ( $E < E_{th}$  for  $\alpha = 0.1$ ), but it does not impair our conclusion, considering that the thermalization efficiency can be higher than the adopted value of 0.1 in an environment where many SNe are exploding (Strickland & Heckman 2009), which will yield a larger  $E$  that is still consistent with  $E_{th}$ . These estimates demonstrate that the observed diffuse thermal gas traced by the highly ionized iron line emission in NGC 6240 is consistent with being heated by SNe shocks in the starburst. The cooling time of this thermal gas is  $\tau_{cool} = E_{th}/Lx \sim 40$  Myr, slightly larger than the starburst duration, which implies that such X-ray bright phase will be short lived once the starburst ceases.

Following Mitsuishi et al. (2011), another useful check is the comparison between the ejected iron mass from SNe and the observed iron mass. Adopting  $M = 8.4 \times 10^{-2} M_{\odot}$  as the ejected iron mass per Type II SN (Iwamoto et al. 1999) and the average SN rate of  $\sim 2 \text{ yr}^{-1}$ , the expected iron mass for the 20 Myr starburst is  $M_{Fe,SB} = 3.4 \times 10^6 M_{\odot}$ , which can easily account for the observed  $M_{Fe,X-ray} = 4.6 \times 10^5 M_{\odot}$  considering not all the iron ejecta are currently X-ray emitting. Therefore this comparison also supports the above scenario that starburst is the origin for the 70 MK gas.

However, the morphological comparison showed some interesting correspondences and differences: (1) in the nuclear region, while Fe XXV and [FeII] both peaks (Figure 9) at the radio nuclei, bright  $\text{H}_2$  emission is observed between the nuclei (Figure 10); (2)  $\text{H}_2$  and the X-ray Fe XXV emission share similar morphology at the ‘arms’ extending southeast and southwest of the southern nucleus (Figure 10), which is not seen with the [FeII] emission. Why do the near-IR  $\text{H}_2$  and the X-ray Fe XXV emission share similar extended morphology, but not [FeII]? We suggest that these differences can be attributed to two aspects. First, there are presence of shocks in different velocity ranges. Secondly, the physical scales of SNR is much localized compared to starburst-driven winds.

van der Werf et al. (1993) suggested that the [FeII] emission in NGC 6240 may originate in shocks associated with SNRs during the starburst in the nuclei, based on the high [FeII]/Br $\gamma$  ratio. When dust grains are destroyed by fast shocks, the Fe abundance in the gas phase is enhanced. Thus it is straightforward to expect that the [FeII] and the highly

ionized Fe emission peaks at the nuclei of NGC 6240, where the intense star formation activities are and young SNR are produced (Tecza et al. 2000; Pollack et al. 2007). Note that Fe XXV in the southern nucleus is  $\sim 3$  times brighter than the northern one (see Figure 10 and Table 2), in agreement with a ratio of  $\sim 2$  found in [FeII] and implying a higher SN rate in the southern nucleus.

From the X-ray perspective, the gas is heated to the high temperature producing the observed hard X-ray emission by the thermalization of the kinetic energy from an ensemble of SNe and winds from massive stars, inside the starburst region, and by internal shocks in the superwind at larger radii (Tomisaka & Ikeuchi 1988, Norman & Ikeuchi 1989, Heckman et al. 1990). Fe XXV emission also peaks at the the radio nuclei and the peaks of [FeII] emission (Figure 9). We can assume that we observe the shocked wind matter, whose temperature then gives us a measure of the shock velocity. For non-radiative, strong shocks in a fully ionized monoatomic gas, the post-shock temperature is  $T_{sh} = 3\mu v_{sh}^2/16k$ , where  $\mu$  is the mean mass per particle and  $k$  is the Boltzmann constant (McKee & Hollenbach 1980). For the observed hot gas ( $kT = 6.15$  keV, or  $\sim 7 \times 10^7$  K), we obtain a shock velocity  $v_{sh} = 2200$  km s $^{-1}$ . Other than shocks driven by the starburst, such high velocity shocks are unlikely to be induced by the merger process in NGC 6240: even in direct collision systems like the Taffy Galaxy (UGC 12914/5), the progenitors collided at  $\sim 600$  km s $^{-1}$  (Braine et al. 2003). The merging galaxies in NGC 6240 have well passed the first encounter, without showing morphology like the ring galaxies exemplifying such a strong direct collision, and the estimated collision velocity from the CO line width is only between 150 and 300 km s $^{-1}$  (Wang et al. 1991; Tecza et al. 2000).

In contrast, the bright H $_2$  emission observed between the nuclei of NGC 6240 has been interpreted to originate in global dissipative shocks resulting from the collisions of the ISM of the merging disk galaxies (Herbst et al. 1990; van der Werf et al. 1993; Max et al. 2005). The shock velocity was constrained to be at most 40 km s $^{-1}$  (van der Werf et al. 1993). However, the fainter large scale ‘arms’ of H $_2$  emission extending SE and SW of the southern nucleus needs a different explanation, as it closely follows the X-ray emission. As fast outflows (several thousand km s $^{-1}$ ) driven by the starburst are expected (e.g., Heckman et al. 1990, Fabbiano et al. 1990; see Veilleux et al. 2005 for a review), this large scale H $_2$  emission can be interpreted as originated from molecular material entrained and shocked by the superwind. The thermal velocity of this 6 keV gas, estimated as the adiabatic sound speed  $v_{th} = (5kT/3\mu m_H)^{1/2} \sim 1260$  km s $^{-1}$  (assuming solar abundance), is much higher than the escape velocity  $v_{esc} = \sqrt{2GM/r}$ , which is  $\sim 210$  km s $^{-1}$  at  $r \sim 1$  kpc using the dynamical mass  $M_{dyn} = 6 \times 10^9 M_\odot$  in Tacconi et al. (1999). Therefore the expanding hot bubble can “blow out” to larger radial distance such as the 5 kpc extent seen here. Following a simple model of a shock propagating in an inhomogeneous ISM in van der Werf et al. (1993), the

high velocity shock ( $v_1 = 2200 \text{ km s}^{-1}$ , see above) in the low density wind responsible for the Fe XXV emission will slow down significantly when encountering a layer of cold molecular gas. The decreased shock speed  $v_2$  can be estimated using the density contrast between the X-ray gas ( $\rho_1 \sim 0.1\eta^{-1/2} \text{ cm}^{-3}$ ) and the molecular cloud ( $\rho_2 \sim 10^4 - 10^5 \text{ cm}^{-3}$ ), following  $v_2/v_1 = \sqrt{\rho_1/\rho_2}$  (Spitzer 1978, Equation [12-39]; note this is different from the shock jump condition). The expected  $v_2 \sim 7 - 20 \text{ km s}^{-1}$  agrees well with the velocity constraint from shock excitation for the observed  $\text{H}_2$  emission (e.g., van der Werf et al. 1993). We have also shown that the hard X-ray emission shares similar characteristics with the optical  $\text{H}\alpha$  emission (Figure 8), with a few filaments and loops that are more apparent in the soft X-rays (Komossa et al. 2003, Wang et al. 2013). The overall picture is that previous models, consisting of multi-temperature, multi-zone thermal plasma powered by starburst can explain the observed emission properties given that the outflows (and consequently shocks) have a large velocity range: the hard X-rays are associated with fast shocks driven by SNe explosions and the soft X-rays/ $\text{H}\alpha$  related to slower shocks associated with mass loaded starburst winds.

More evidence supporting this scenario also comes from the presence of high velocity  $\text{H}_2$  and  $\text{H}\alpha$  emission in the ‘arms’ region, based on prominent wings in the  $\text{H}_2$  1-0 S(1) line (with full width at zero intensity of  $\sim 1600 \text{ km s}^{-1}$ ; van der Werf et al. 1993; Engel et al. 2010) and  $\text{H}\alpha$  line profile (Heckman et al. 1990), tracing the ambient gas entrained and shocked by the superwind. In a very recent CO(1-0) interferometry observation of NGC 6240, Feruglio et al. (2013) further identified evidence for a shock wave that propagates eastward from the nuclei. One of the resolved structures of blue shifted CO emission is spatially coincident with the SE  $\text{H}_2$  filament (Max et al. 2005), which is also associated with  $\text{H}\alpha$  and soft X-ray emission. The derived kinetic power of the outflowing CO gas is  $6 \times 10^{42} \text{ erg s}^{-1}$ , with an estimated age  $> 2 \times 10^7$  years. This implies a total kinetic energy of  $E_{kin} = 3.8 \times 10^{57}$  ergs. Recall that the available kinetic input from the multiple SNe explosions during the starburst is  $4 \times 10^{58}$  ergs ( $10^{51}$  ergs per SN  $\times 2 \text{ yr}^{-1} \times 2 \times 10^7 \text{ yr}$ ), there seems no deficit in the energy budget. However, we cannot yet draw conclusion that no additional energy injection is required, until a full tally of the bulk kinetic energy and thermal energy of the outflowing gas in other phases is available for NGC 6240. Under the assumption that the 70 million K gas is volume filling ( $\eta = 100\%$ ; Strickland & Stevens 2000), its  $E_{th}$  would exceed the available kinetic energy provided by the recent starburst by  $2.5 \times 10^{58}$  ergs, implying additional kinetic power input such as from an AGN outflow or multiple star forming episodes. In fact, the thermal energy content in the large scale ( $\sim 100 \text{ kpc}$ ) soft X-ray halo ( $kT = 0.65 \text{ keV}$ ) in NGC 6240 identified by Nardini et al. (2013) is estimated to be  $4.9 \times 10^{58}$  ergs, which hints at additional energy input from a widespread, enhanced star formation proceeding at steady rate over  $\sim 200 \text{ Myr}$  (Nardini et al. 2013) besides the most recent nuclear starburst.

Lastly, we note that a good spatial correlation is also expected if the  $\text{H}_2$  emission is

excited by localized X-ray irradiation of molecular clouds (Draine & Woods 1990). However, this was concluded unlikely (van der Werf et al. 1993), since the required SN rate of  $7 \text{ yr}^{-1}$  (Draine & Woods 1991) is much higher than the inferred rate from radio, infrared, and our X-ray measurement. Thus we conclude that propagation of fast shocks originated in the starburst driven wind into the ambient dense gas can account for the large scale X-ray and  $\text{H}_2$  morphological correspondence.

## 5. Conclusions

Combining new and archival *Chandra* observations of NGC 6240, we have obtained the deepest X-ray image of the central  $r = 5 \text{ kpc}$  ( $10''$ ) of the merging ULIRG NGC 6240 with sub-arcsecond resolution. Studying the hard X-ray emission centered at Fe K complex and comparing to images in other wavebands, here for the first time we clearly resolved hard extended emission with its extension established, and assessed the nuclei contribution to the hard emission separately. Such a hard extended emission was predicted to be the innermost manifestation of superwinds. So far, the superwind nature of NGC 6240 had been studied mostly in the  $\text{H}\alpha$ , molecular gas, and soft X-rays. We summarize our findings as follows:

1. The X-ray emission from the pair of active nuclei and the diffuse hot gas is resolved in detail. Extended X-ray emission from  $kT \sim 6 \text{ keV}$  ( $\sim 70$  million K) hot gas was found over a spatial scale of 5 kpc, indicating the presence of fast shocks with velocity of  $\sim 2200 \text{ km s}^{-1}$ .
2. The observed luminosity of the 70 million K temperature gas is  $L_{0.5-8\text{keV}} = 5.3 \times 10^{41} \text{ erg s}^{-1}$ , with a total mass of  $M_{hot} = 1.8 \times 10^8 M_\odot$  and thermal energy  $E_{th} = 6.5 \times 10^{57} \text{ ergs}$ , assuming a filling factor of 1% for the hot gas. The total iron mass in the highly ionized plasma is  $M_{\text{FeXXV}} = 4.6 \times 10^5 M_\odot$ . Both the energetics and the iron mass in the hot gas are commensurate with the expected injection from the starburst, assuming an average SN rate of  $2 \text{ yr}^{-1}$  that is in agreement with its high star formation rate and estimates from non-thermal radio emission and [FeII] luminosity.
3. The spatial distribution of the highly ionized gas emitting Fe XXV peaks together with the [FeII] emission around the radio nuclei, associated with the high concentration of young SNRs during the nuclear starburst. The extended Fe XXV emission shows a remarkable correspondence to the large scale morphology of  $\text{H}_2(1-0) \text{ S}(1)$  line emission and  $\text{H}\alpha$  filaments. Propagation of fast shocks originated in the starburst driven wind into the ambient dense gas can account for this morphological correspondence. The Fe

I  $K\alpha$  emission peaks at the active nuclei. No evidence for fluorescent Fe I emission is found in the CO filament connecting the two nuclei.

Although the above superwind scenario accounts for the extended hard X-ray emission and observational evidence in other wavebands, we cannot yet rule out additional energy injection in the central region of NGC 6240 (e.g., heating by an AGN outflow). Given the poorly constrained volume filling factor of the X-ray emitting gas, the thermal energy of the hot gas may exceed the available kinetic energy provided by the SNe explosions during the most recent starburst ( $E_{th} - E_{SB} = 2.5 \times 10^{58}$  ergs for  $\eta = 100\%$ ), implying additional energy input such as from an AGN outflow or more complex star formation activities besides the recent nuclear starburst (see discussion in Nardini et al. 2013). A full tally of the bulk kinetic energy and thermal energy of the outflowing gas in other phases is crucial for the evaluation of energy budget in the NGC 6240 system. We will further characterize the soft X-ray emission within the central 15 kpc in this merging galaxy in a forthcoming paper (Wang et al. in preparation).

We acknowledge the anonymous referee for the careful reading and constructive suggestions. This work is supported by NASA grant GO1-12123X (PI: Fabbiano). We acknowledge support from the CXC, which is operated by the Smithsonian Astrophysical Observatory (SAO) for and on behalf of NASA under Contract NAS8-03060. J.W. acknowledges support from the Northwestern University CIERA Fellowship. This material is based upon work supported in part by the National Science Foundation Grant No. 1066293 and the hospitality of the Aspen Center for Physics. M.K. is a member of CXC. Some of the data presented here were obtained at the W. M. Keck Observatory, which is operated as a scientific partnership among the California Institute of Technology, the University of California and NASA. The W. M. Keck Observatory and the Keck II AO system were made possible by the generous financial support of the W.M. Keck Foundation. This research has made use of data obtained from the *Chandra* Data Archive, and software provided by the CXC in the application packages CIAO. This work has made use of the Hubble Legacy Archive, which is a collaboration between the Space Telescope Science Institute (STScI/NASA), the Space Telescope European Coordinating Facility (ST-ECF/ESA) and the Canadian Astronomy Data Centre (CADK/NRC/CSA).

*Facilities:* CXO (ACIS)

## REFERENCES

Beswick, R. J., Pedlar, A., Mundell, C. G., & Gallimore, J. F. 2001, MNRAS, 325, 151

- Boller, T., Keil, R., Hasinger, G., et al. 2003, *A&A*, 411, 63
- Braine, J., Davoust, E., Zhu, M., et al. 2003, *A&A*, 408, L13
- Bush, S. J., Wang, Z., Karovska, M., & Fazio, G. G. 2008, *ApJ*, 688, 875
- Chevalier, R. A., & Clegg, A. W. 1985, *Nature*, 317, 44
- Colbert, E. J. M., Wilson, A. S., & Bland-Hawthorn, J. 1994, *ApJ*, 436, 89
- Colina, L., Pereira-Santaella, M., Alonso-Herrero, A., Bedregal, A. G., & Arribas, S. 2012, *ApJ*, 749, 116
- Downes, D., Solomon, P. M., & Radford, S. J. E. 1993, *ApJ*, 414, L13
- Draine, B. T., & Woods, D. T. 1990, *ApJ*, 363, 464
- Draine, B. T., & Woods, D. T. 1991, *ApJ*, 383, 621
- Engel, H., Davies, R. I., Genzel, R., et al. 2010, *A&A*, 524, A56
- Esch, D. N., Connors, A., Karovska, M., & van Dyk, D. A. 2004, *ApJ*, 610, 1213
- Fabbiano, G., Heckman, T., & Keel, W. C. 1990, *ApJ*, 355, 442
- Feruglio, C., Fiore, F., Maiolino, R., et al. 2013, *A&A*, 549, A51
- Garmire, G. P., Bautz, M. W., Ford, P. G., Nousek, J. A., & Ricker, G. R., Jr. 2003, *Proc. SPIE*, 4851, 28
- Grevesse, N., & Sauval, A. J. 1998, *Space Sci. Rev.*, 85, 161
- Grimes, J. P., Heckman, T., Strickland, D., & Ptak, A. 2005, *ApJ*, 628, 187
- Heckman, T. M., Armus, L., & Miley, G. K. 1990, *ApJS*, 74, 833
- Herbst, T. M., Graham, J. R., Tsutsui, K., et al. 1990, *AJ*, 99, 1773
- Hollenbach, D., & McKee, C. F. 1989, *ApJ*, 342, 306
- Hughes, J. P., Hayashi, I., & Koyama, K. 1998, *ApJ*, 505, 732
- Huo, Z. Y., Xia, X. Y., Xue, S. J., Mao, S., & Deng, Z. G. 2004, *ApJ*, 611, 208
- Iono, D., Wilson, C. D., Takakuwa, S., et al. 2007, *ApJ*, 659, 283
- Iwamoto, K., Brachwitz, F., Nomoto, K., et al. 1999, *ApJS*, 125, 439

- Iwasawa, K., & Comastri, A. 1998, MNRAS, 297, 1219
- Iwasawa, K., Sanders, D. B., Evans, A. S., et al. 2005, MNRAS, 357, 565
- Iwasawa, K., Sanders, D. B., Evans, A. S., et al. 2009, ApJ, 695, L103
- Karovska, M., Schlegel, E., Hack, W., Raymond, J. C., & Wood, B. E. 2005, ApJ, 623, L137
- Karovska, M., Carilli, C. L., Raymond, J. C., & Mattei, J. A. 2007, ApJ, 661, 1048
- Komatsu, E., Smith, K. M., Dunkley, J., et al. 2011, ApJS, 192, 18
- Komossa, S., Burwitz, V., Hasinger, G., et al. 2003, ApJ, 582, L15
- Lehmer, B. D., Alexander, D. M., Bauer, F. E., et al. 2010, ApJ, 724, 559
- Li, J., Kastner, J. H., Prigozhin, G. Y., & Schulz, N. S. 2003, ApJ, 590, 586
- Lira, P., Ward, M. J., Zezas, A., & Murray, S. S. 2002, MNRAS, 333, 709
- Lucy, L. B. 1974, AJ, 79, 745
- Matt, G., Fabian, A. C., Guainazzi, M., et al. 2000, MNRAS, 318, 173
- Max, C. E., Canalizo, G., Macintosh, B. A., et al. 2005, ApJ, 621, 738
- Max, C. E., Canalizo, G., & de Vries, W. H. 2007, Science, 316, 1877
- McKee, C. F., & Hollenbach, D. J. 1980, ARA&A, 18, 219
- Medling, A. M., Ammons, S. M., Max, C. E., et al. 2011, ApJ, 743, 32
- Mitsuishi, I., Yamasaki, N. Y., & Takei, Y. 2011, ApJ, 742, L31
- Moorwood, A. F. M., & Oliva, E. 1988, A&A, 203, 278
- Nardini, E., Wang, J., Fabbiano, G., et al. 2013, ApJ, 765, 141
- Netzer, H., Lemze, D., Kaspi, S., et al. 2005, ApJ, 629, 739
- Norman, C. A., & Ikeuchi, S. 1989, ApJ, 345, 372
- Palmeri, P., Mendoza, C., Kallman, T. R., Bautista, M. A., & Meléndez, M. 2003, A&A, 410, 359
- Pietsch, W., Roberts, T. P., Sako, M., et al. 2001, A&A, 365, L174

- Pollack, L. K., Max, C. E., & Schneider, G. 2007, *ApJ*, 660, 288
- Ptak, A., Heckman, T., Levenson, N. A., Weaver, K., & Strickland, D. 2003, *ApJ*, 592, 782
- Richings, A. J., Fabbiano, G., Wang, J., & Roberts, T. P. 2010, *ApJ*, 723, 1375
- Rosenberg, M. J. F., van der Werf, P. P., & Israel, F. P. 2012, *A&A*, 540, A116
- Sanders, D. B., & Mirabel, I. F. 1996, *ARA&A*, 34, 749
- Shu, X. W., Yaqoob, T., & Wang, J. X. 2011, *ApJ*, 738, 147
- Smith, R. K., Brickhouse, N. S., Liedahl, D. A., & Raymond, J. C. 2001, *ApJ*, 556, L91
- Suchkov, A. A., Balsara, D. S., Heckman, T. M., & Leitherer, C. 1994, *ApJ*, 430, 511
- Strickland, D. K., & Stevens, I. R. 2000, *MNRAS*, 314, 511
- Strickland, D. K., & Heckman, T. M. 2007, *ApJ*, 658, 258
- Strickland, D. K., & Heckman, T. M. 2009, *ApJ*, 697, 2030
- Schulz, H., Komossa, S., Berghofer, T. W., & Boer, B. 1998, *A&A*, 330, 823
- Spitzer, L. 1978, *Physical Processes in the Interstellar Medium*, New York Wiley-Interscience
- Tacconi, L. J., Genzel, R., Tecza, M., et al. 1999, *ApJ*, 524, 732
- Tecza, M., Genzel, R., Tacconi, L. J., et al. 2000, *ApJ*, 537, 178
- Thornton, K., Gaudlitz, M., Janka, H.-T., & Steinmetz, M. 1998, *ApJ*, 500, 95
- Tomisaka, K., & Ikeuchi, S. 1988, *ApJ*, 330, 695
- U, V., Wang, Z., Sanders, D., et al. 2011, *Galaxy Evolution: Infrared to Millimeter Wavelength Perspective*, 446, 97
- van der Werf, P. P., Genzel, R., Krabbe, A., et al. 1993, *ApJ*, 405, 522
- Veilleux, S., Cecil, G., & Bland-Hawthorn, J. 2005, *ARA&A*, 43, 769
- Wang, J., Fabbiano, G., Karovska, M., et al. 2009, *ApJ*, 704, 1195
- Wang, J., Fabbiano, G., Karovska, M., Elvis, M., & Risaliti, G. 2012, *ApJ*, 756, 180
- Wang, Z., Scoville, N. Z., & Sanders, D. B. 1991, *ApJ*, 368, 112

Whittle, M., & Wilson, A. S. 2004, *AJ*, 127, 606

Yun, M. S., & Carilli, C. L. 2002, *ApJ*, 568, 88

Zacharias, N., Monet, D. G., Levine, S. E., et al. 2004, *Bulletin of the American Astronomical Society*, 36, 1418

Table 1: Chandra ACIS Observation Log for NGC 6240.

ObsID	Date	Exposure (ks)	Instrument	Data Mode	Roll Angle (°)
1590	Feb-22-2002	37	ACIS-S	Faint	246.2
6909	May-11-2006	143	HETG/ACIS-S	VFaint	129.9
6908	May-16-2006	159	HETG/ACIS-S	VFaint	138.1
12713	May-31-2011	146	ACIS-S	Faint	167.2
Total Effective Exposure* (ks) ...		363			

\* The effective exposure time for the *Chandra* HETG zeroth order image refers to the equivalent exposure needed if the data were taken with direct *Chandra* ACIS imaging, calculated by comparing its effective area to that of ACIS imaging without grating.

Table 2: Chandra ACIS Measurements of the Complex Fe K Lines in NGC 6240.

Region	Counts (5.5-8 keV)		Fe I	Fe XXV	Fe XXVI
Nuc-N	908	Energy (keV) *	6.26±0.01	6.54±0.03	6.86±0.04
		Flux **	10.7±0.8	2.2±0.5	1.6±0.6
		EW (eV)	645 <sup>+680</sup> <sub>-18</sub>	73 <sup>+36</sup> <sub>-24</sub>	105 <sup>+134</sup> <sub>-32</sub>
Nuc-S	2096	Energy (keV) *	6.23±0.01	6.46±0.01	6.68 <sup>+0.03</sup> <sub>-0.01</sub>
		Flux **	13.5±0.9	8.0±0.8	4.5±0.7
		EW (eV)	342±30	154 <sup>+15</sup> <sub>-20</sub>	115 <sup>+24</sup> <sub>-20</sub>
$r \leq 10''$	4856	Energy (keV) *	6.25±0.01	6.51 <sup>+0.01</sup> <sub>-0.02</sub>	6.74±0.02
		Flux **	28.4 <sup>+1.3</sup> <sub>-1.2</sub>	16.2±1.1	4.3 <sup>+0.8</sup> <sub>-1.3</sub>
		EW (eV)	359±22	170 <sup>+8</sup> <sub>-4</sub>	53±14
$r \leq 70''$ ( <i>XMM</i> ) <sup>†</sup>	...	Energy (keV) *	6.26±0.02	6.52±0.02	6.84±0.04
		Flux **	26±8	18±7	9±7
		EW (eV)	300±100	220±90	120±90

\* Observed energies of the line centers.

\*\* Photon flux in the unit of  $10^{-6}$  photons  $s^{-1}$   $cm^{-2}$ .

<sup>†</sup> *XMM*-Newton EPIC measured FeK line complex from Boller et al.(2003). Because of the lower angular resolution of *XMM*-Newton, the spectrum is extracted using a circular region with radius of  $70''$ .

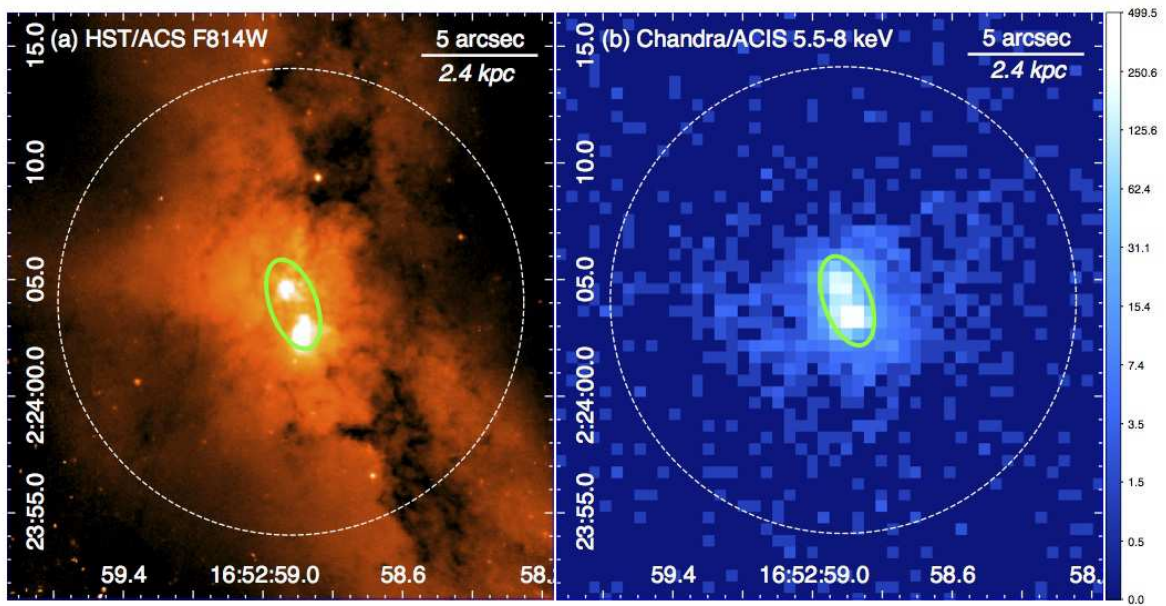


Fig. 1.— (a) HST/ACS F814W image of the central  $25'' \times 25''$  (12 kpc across) region of NGC 6240, showing the disturbed optical disk. (b) The Chandra ACIS image (5.5-8 keV) of the same region extracted from the merged data. The white circles ( $r = 10''$ ) mark the spatial extent of the hard X-ray emission. The green ellipses ( $4'' \times 2''$ ) enclose the two nuclei.

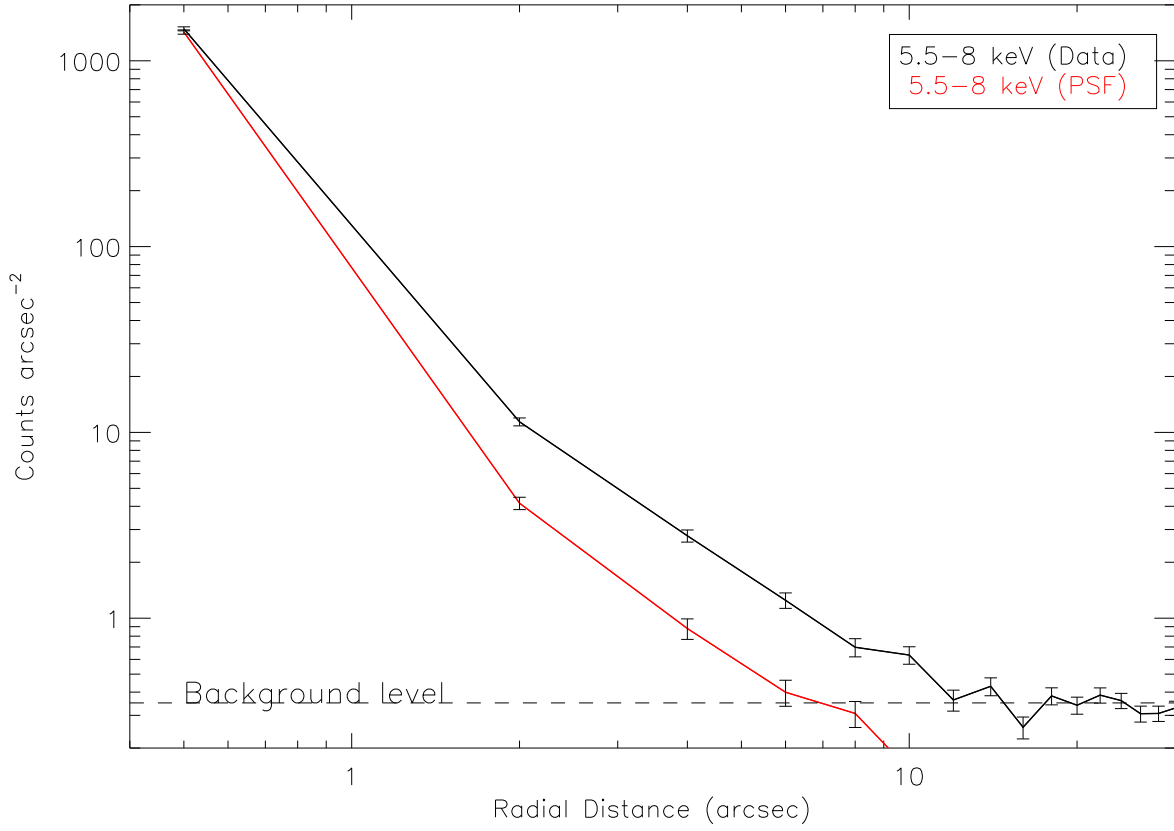


Fig. 2.— Comparison between the observed surface brightness profile (black; full merged data) and that expected from the Chandra PSF for the 5.5-8 keV emission (red). Note the presence of significant hard X-ray emission reaching  $r \sim 10''$  radial distance.

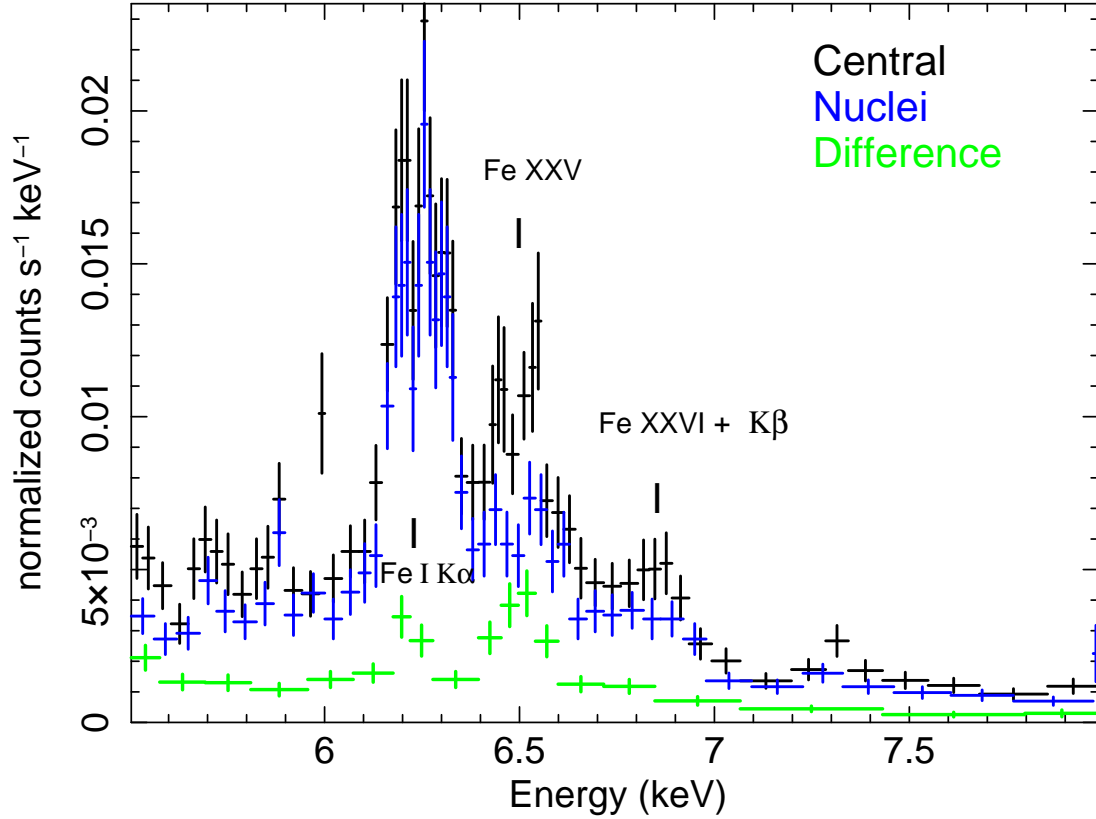


Fig. 3.— Comparison between the X-ray spectra for the dual AGN region (shown in blue; extracted from the ellipse in Figure 1) and the 10 arcsec radius region (shown in black; extracted from the circle in Figure 1) including both the diffuse and AGN emission. The X-ray spectrum for the central region excluding the nuclei is also shown (green) to illustrate the spectral difference and its flux level. The energy scale is observed (not rest frame).

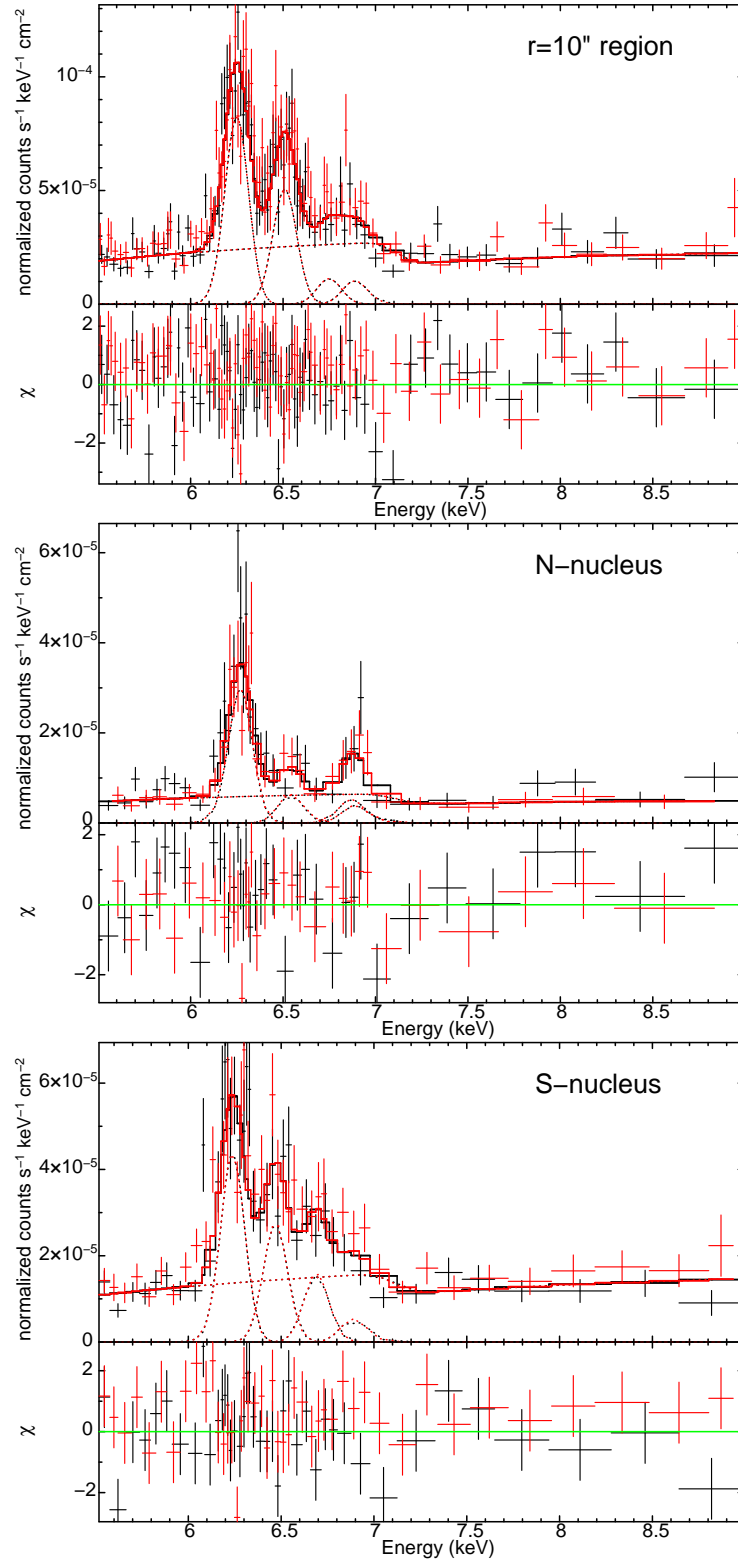


Fig. 4.— Top to bottom: ACIS spectra and fits for the extended central emission, the northern nucleus, and the southern nucleus. Both ACIS data (black) and HETG (red) zeroth order data were used. The model components are also shown as dashed lines (see Table 2).

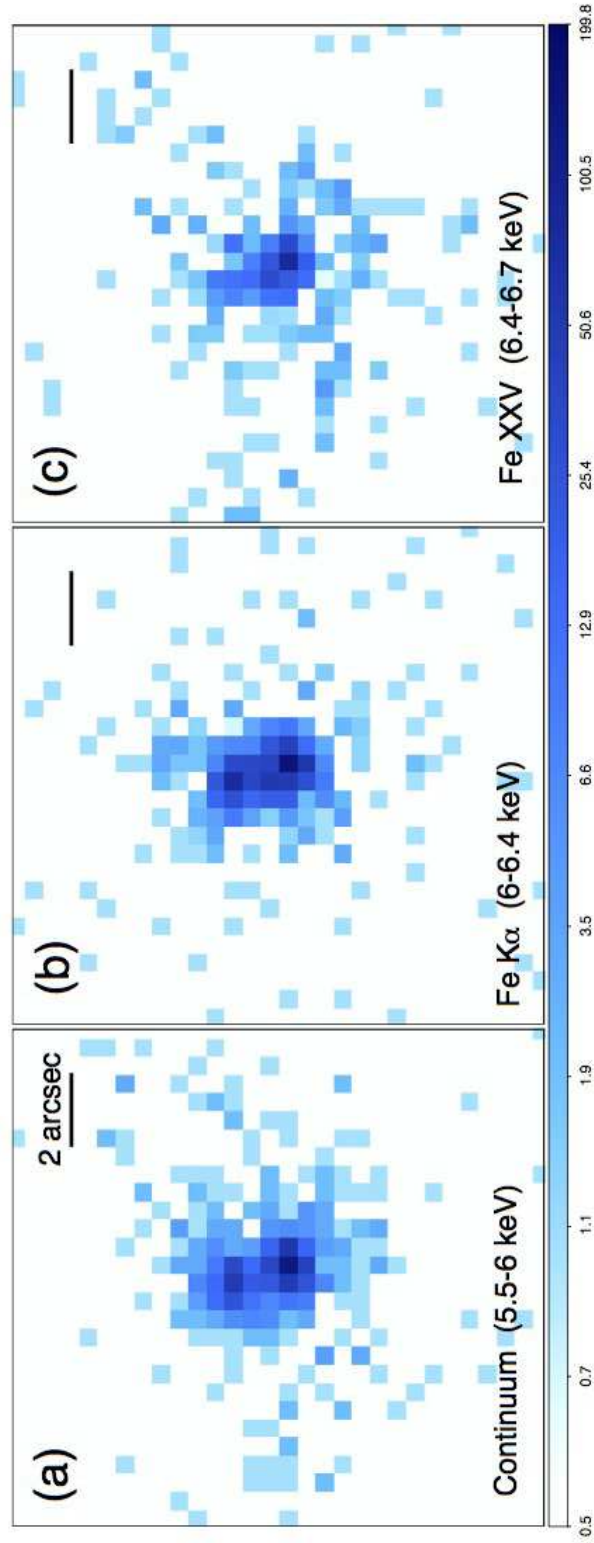


Fig. 5.— Narrow band ACIS images: (a) the 5.5-6 keV continuum band; (b) Fe K $\alpha$  line (6-6.4 keV); and (c) Fe XXV line (6.4-6.7 keV). The latter two images were continuum-subtracted (see text).

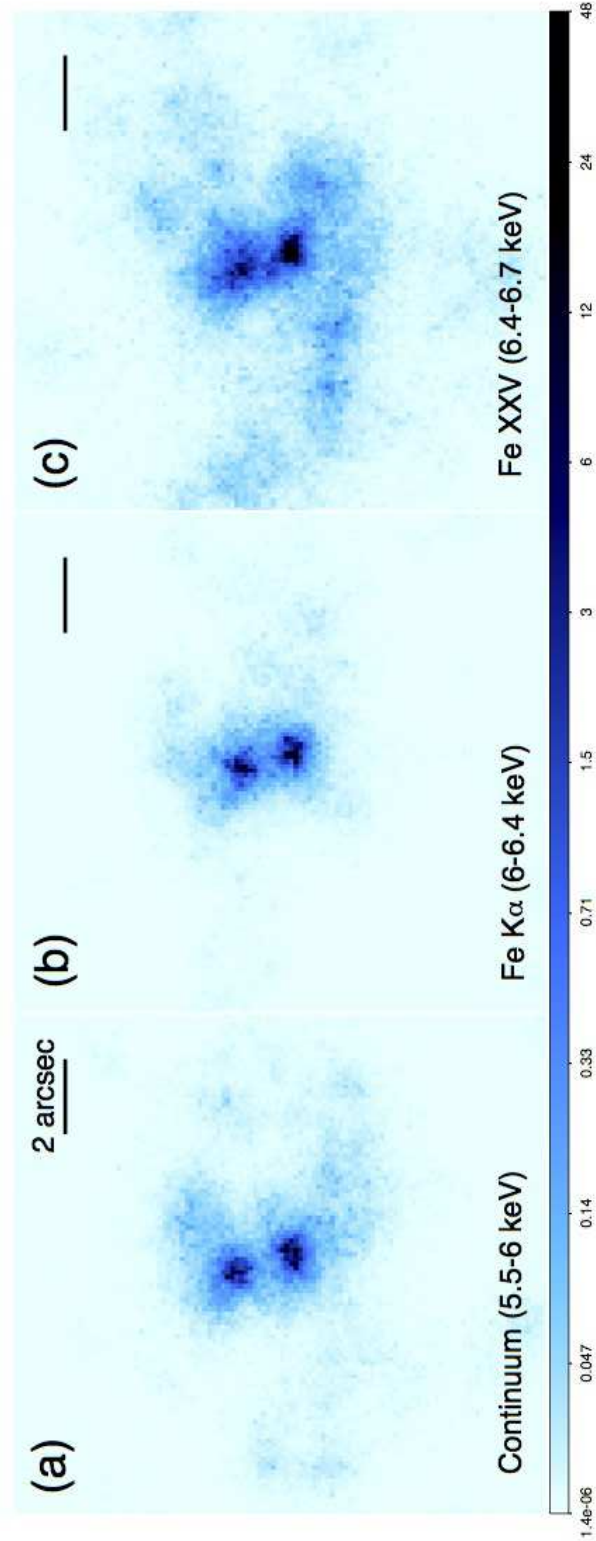


Fig. 6.— Narrow band ACIS images, with EMC2 PSF-deconvolution applied: (a) the continuum band (5.5-6 keV); (b) line image for the neutral Fe K $\alpha$  line (6-6.4 keV); and (c) the Fe XXV (6.4-6.7 keV).

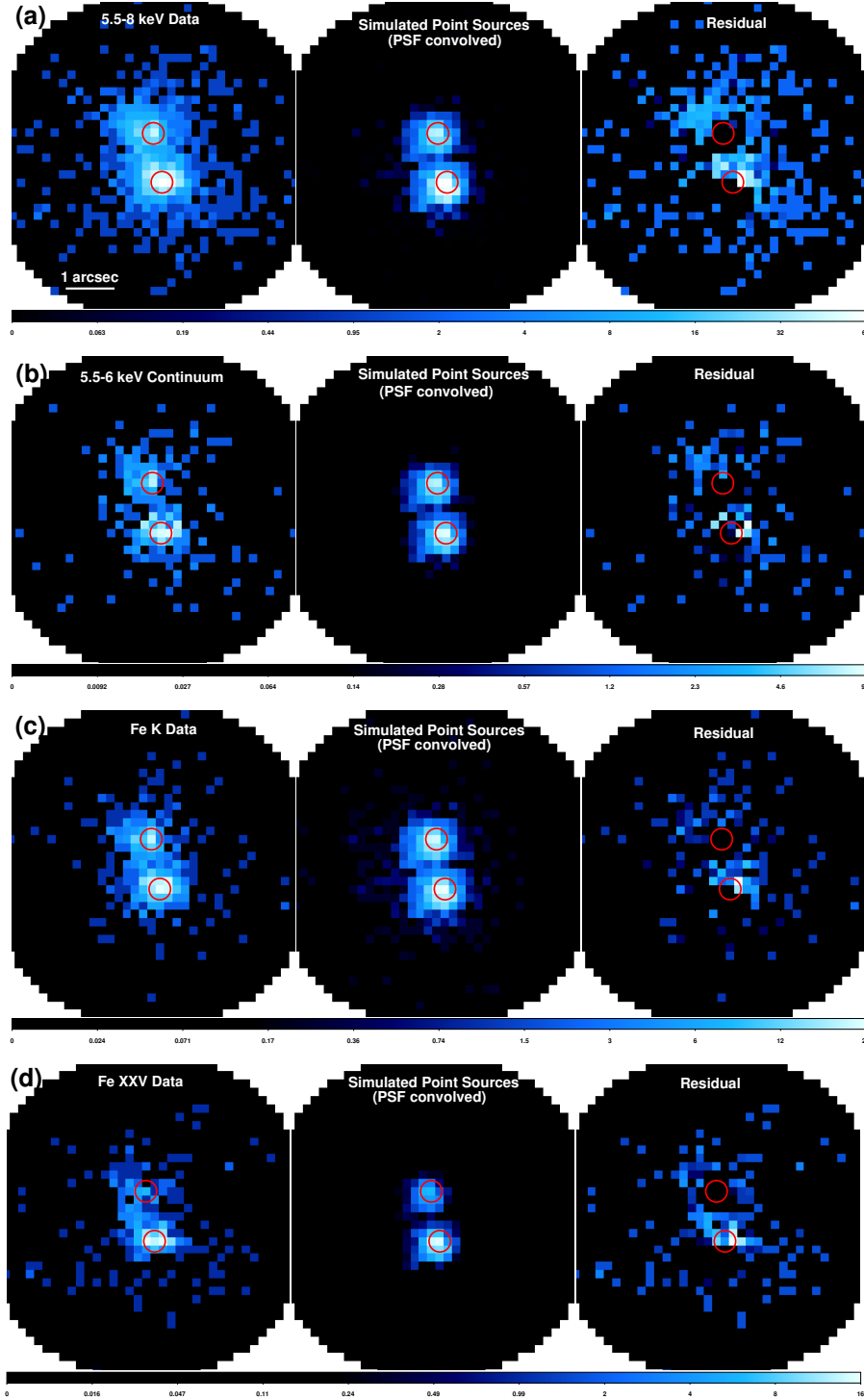


Fig. 7.— 2-D image fitting of the innermost nuclear region in (a) 5.5-8 keV (b) 5.5-6 keV (continuum) (c) 6.0-6.4 keV (Fe I) (d) 6.4-6.7 keV (Fe XXV). For each band, the observed image, simulated pair of point sources representing the double nuclei, and the residual emission are shown. The two circles mark the compact radio nuclear sources (Colbert et al. 1994).

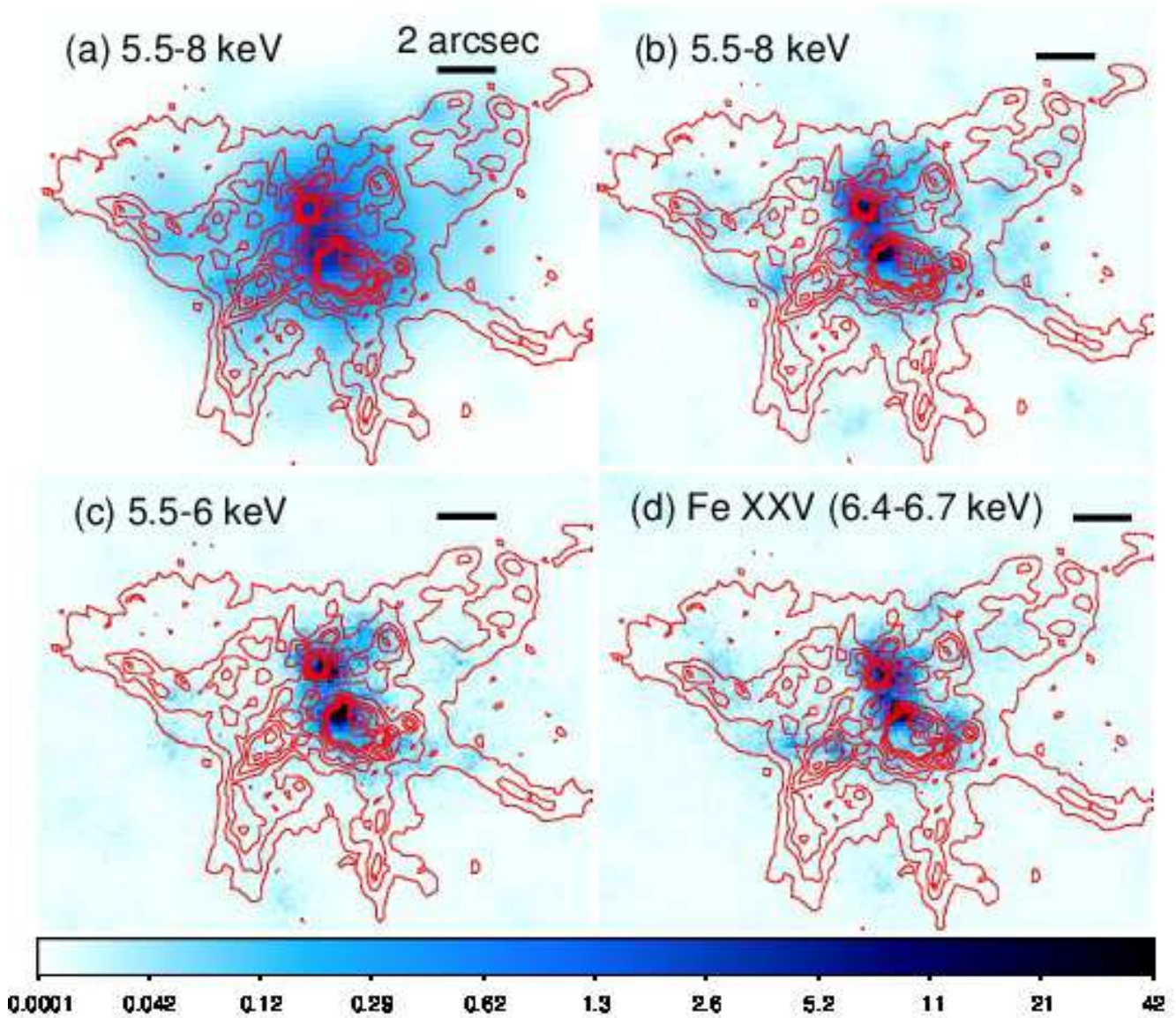


Fig. 8.— (a) The adaptively smoothed 5.5-8 keV ACIS image (in 1/2 pixel binning) overlaid with the HST/WFPC2 H $\alpha$  contours (Lira et al. 2002). (b) The PSF-deconvolved 5.5-8 keV image overlaid with the same H $\alpha$  contours. (c) The PSF-deconvolved continuum band (5.5-6 keV) image (Figure 6a) overlaid with the same H $\alpha$  contours. (d) The PSF-deconvolved Fe XXV image (Figure 6c) overlaid with the same H $\alpha$  contours.

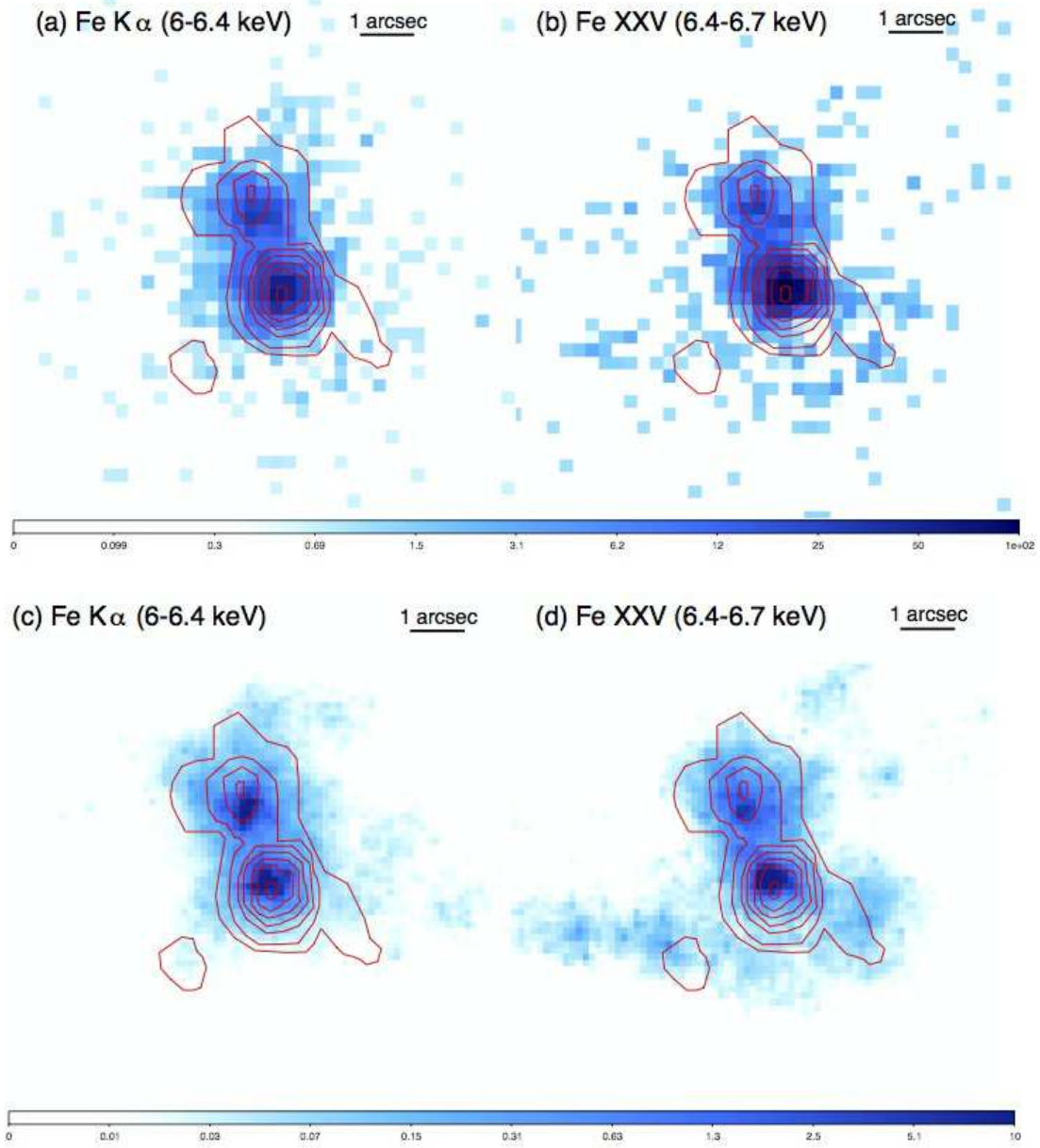


Fig. 9.— The near-IR [FeII] 1.64  $\mu\text{m}$  contours (van der Werf et al. 1993) overlaid on: (a) raw (6-6.4 keV) Fe I K $\alpha$  emission; (b) raw (6.4-6.7 keV) Fe XXV line emission; (c) same as (a) but with EMC2 deconvolution; (d) same as (b) but with EMC2 deconvolution.

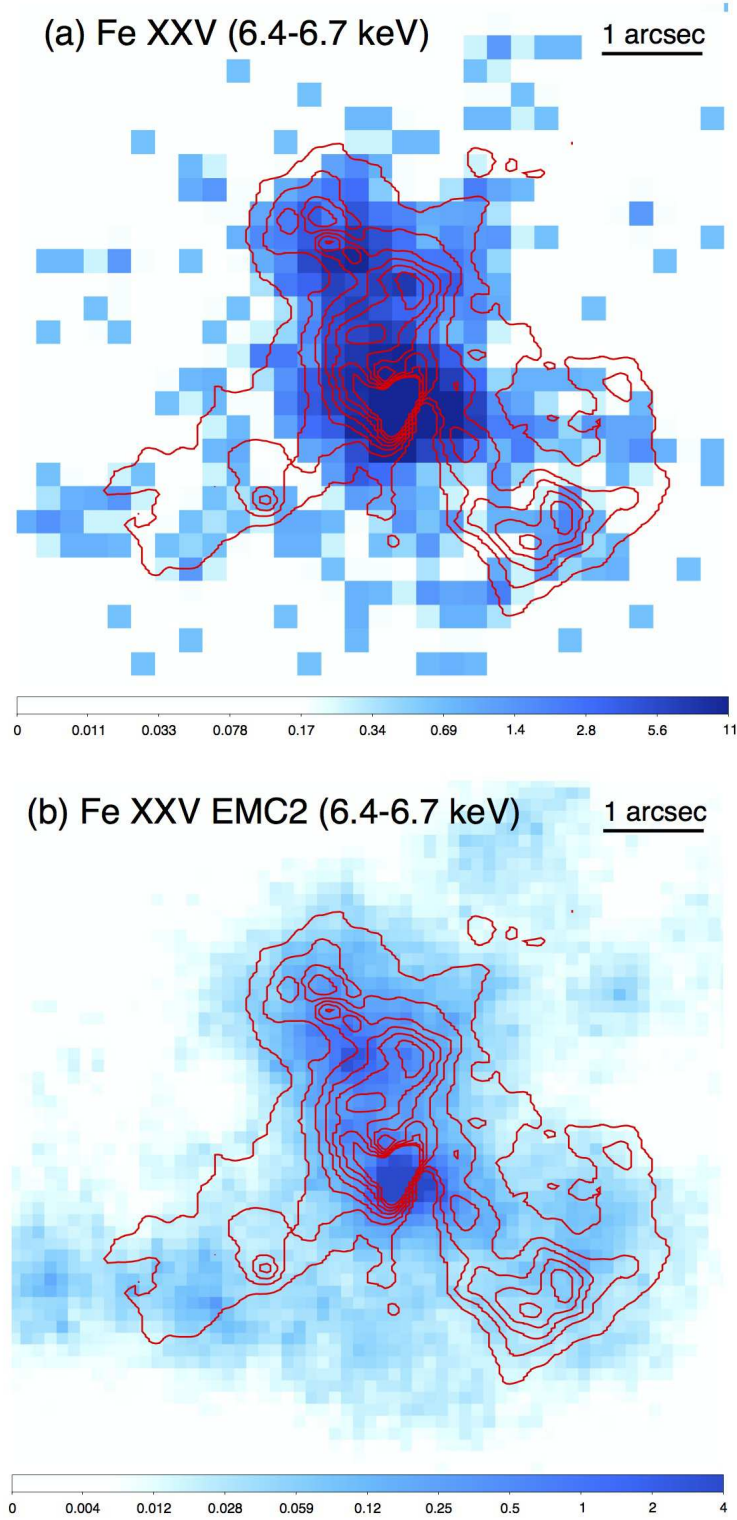


Fig. 10.— (a) The FeXXV line emission image overlaid with the contours of H<sub>2</sub>(1-0) 2.12 μm emission (Max 2005); (b) PSF-deconvolved Fe XXV line emission image with the same H<sub>2</sub> contours.

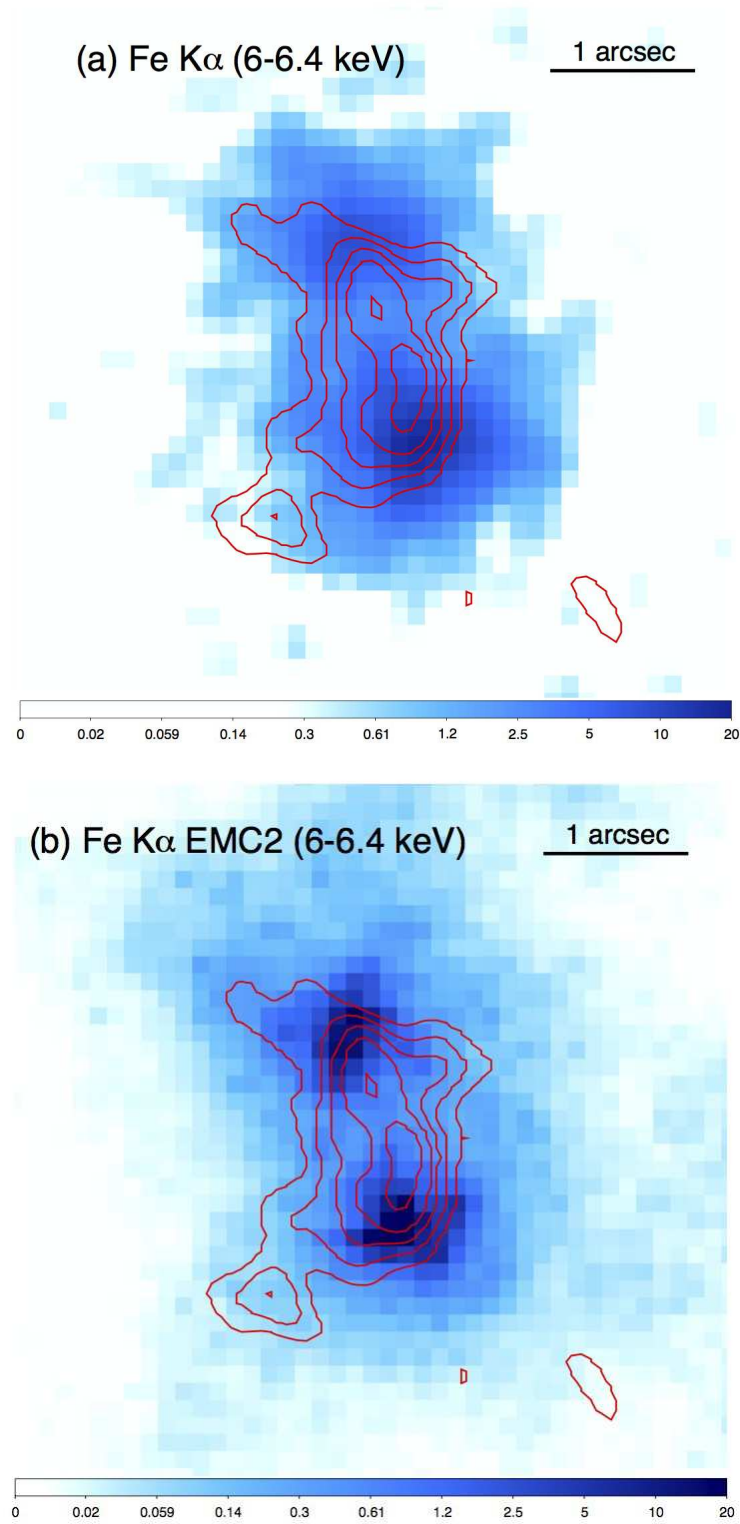


Fig. 11.— (a) The Fe K $\alpha$  line emission image overlaid with the contours of SMA CO(3-2) emission (U et al. 2011); (b) PSF-deconvolved Fe K $\alpha$  line emission image with the same CO contours.

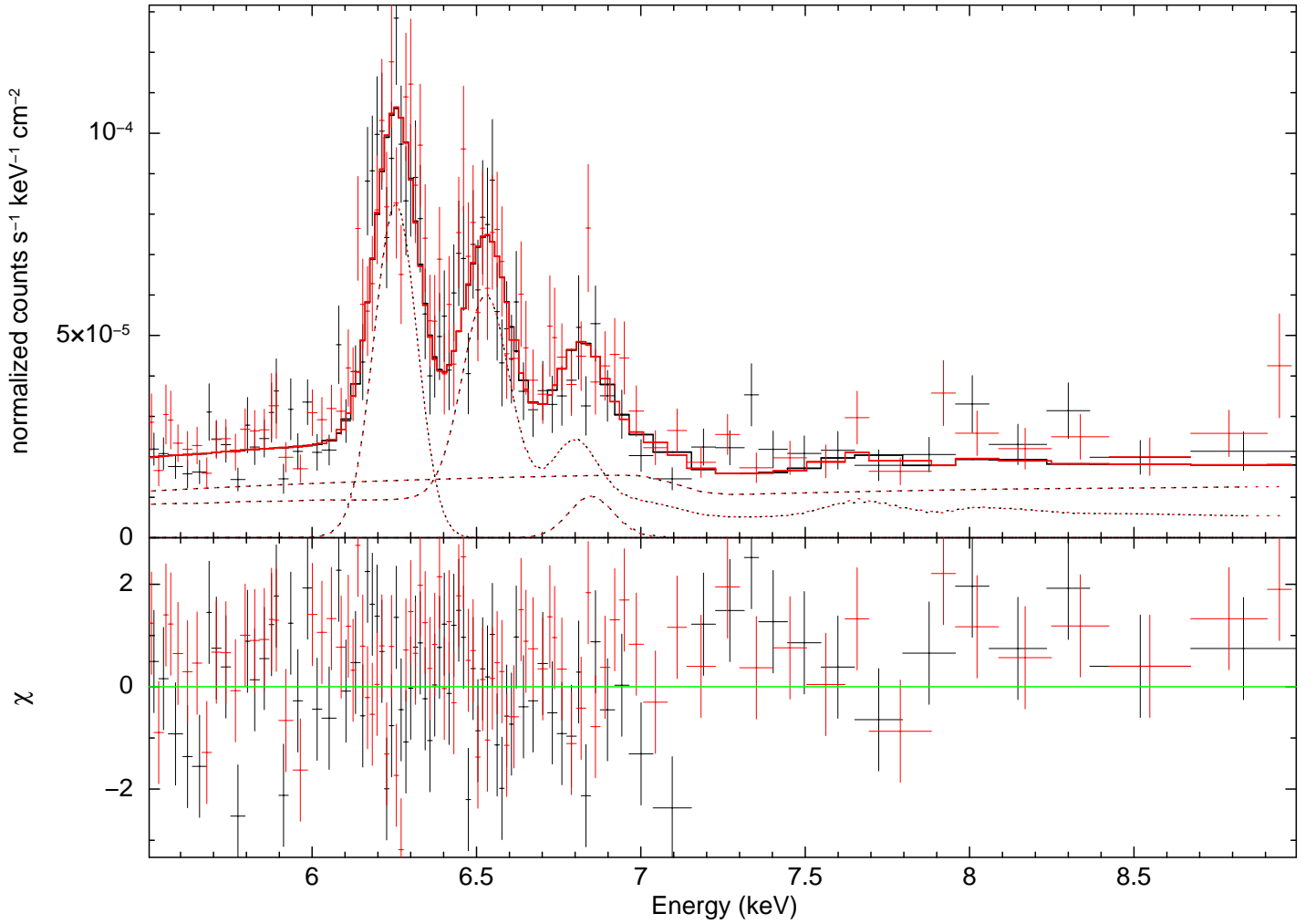


Fig. 12.— The X-ray spectra of the NGC 6240  $r = 10''$  central emission (black: ACIS data; red: HETG zeroth order data) and the fit using thermal plasma model for the hot gas (see the text in § 3.5).

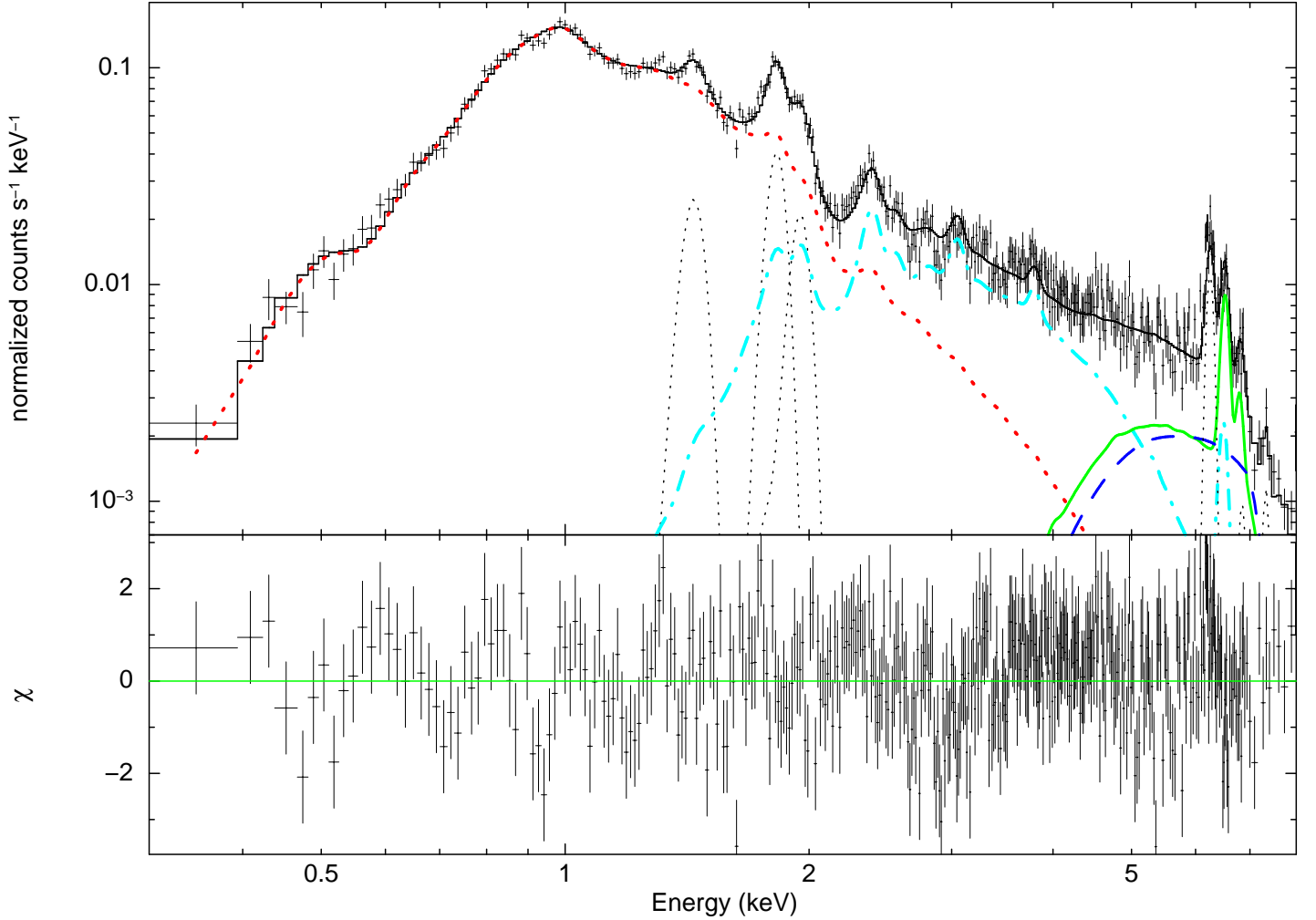


Fig. 13.— The broad band (0.3–8 keV) ACIS spectrum of the NGC 6240  $r = 10''$  central emission (black line: the total model emission). The best fit model components are overplotted including three thermal components for the hot gas, two with lower temperature (red dotted line: the  $kT_1=1.03$  keV component, cyan dash-dotted line:  $kT_2 = 1.56$  keV) and one with a high temperature ( $kT_3 = 6.0$  keV) emitting the Fe XXV line (green solid line). The absorbed powerlaw component (blue dashed line) represents the any scattered nuclear continuum and four narrow gaussian lines correspond to the MgXII, SiXIV, SXVI and FeI  $K\alpha$  lines (see the text in § 3.5).